Polarimetric calibration of spaceborne and airborne multifrequency SAR data for scattering-based characterization of manmade and natural features

Kumar, Shashi; Babu, Arun; Agrawal, Shefali; Asopa, Udit; Shukla, Shashwat; Maiti, Abhisek

DOI
10.1016/j.asr.2021.02.023

Publication date
2022

Document Version
Final published version

Published in
Advances in Space Research

Citation (APA)
Kumar, S., Babu, A., Agrawal, S., Asopa, U., Shukla, S., & Maiti, A. (2022). Polarimetric calibration of spaceborne and airborne multifrequency SAR data for scattering-based characterization of manmade and natural features. *Advances in Space Research*, *69*(4), 1684-1714. https://doi.org/10.1016/j.asr.2021.02.023

Available online at www.sciencedirect.com

ScienceDirect

Advances in Space Research 69 (2022) 1684–1714

ADVANCES IN SPACE RESEARCH (a COSPAR publication)

www.elsevier.com/locate/asr

Polarimetric calibration of spaceborne and airborne multifrequency SAR data for scattering-based characterization of manmade and natural features

Shashi Kumar [a,*], Arun Babu [a,b], Shefali Agrawal [a], Udit Asopa [a,c], Shashwat Shukla [a,c,d], Abhisek Maiti [a,d]

[a] *Indian Institute of Remote Sensing (IIRS), Indian Space Research Organisation (ISRO), 04 Kalidas Road, Dehradun 248001, Uttarakhand, India*
[b] *Microwaves and Radar Institute of German Aerospace Center (DLR), Oberpfaffenhofen 82234, Germany*
[c] *Faculty of Civil Engineering and Geosciences, Delft University of Technology (TU Delft), 2600 GB, The Netherlands*
[d] *Faculty of Geo-Information Science and Earth Observation (ITC), University of Twente, Enschede 7514 AE, The Netherlands*

Received 12 November 2020; received in revised form 18 January 2021; accepted 13 February 2021
Available online 25 February 2021

Abstract

The Polarimetric Synthetic Aperture Radar (PolSAR) systems use electromagnetic radiations of different polarizations in the microwave frequency to collect the scattering information from targets on the Earth. Nevertheless, as with any other electronic device, the PolSAR systems are also not ideal and subjected to distortions. The most important of these distortions are the polarimetric distortions caused due to the channel imbalance, phase bias, and crosstalk between the different polarization channels. For the spaceborne PolSAR systems, the Earth's ionosphere also contributes to an additional polarimetric distortion known as the Faraday rotation. An effort was made in this study to perform the polarimetric calibration of the Quad-pol and Compact-pol PolSAR datasets acquired using different airborne and spaceborne PolSAR systems to estimate and minimize these polarimetric distortions. The investigation was also done to analyze the impact of these polarimetric distortions on the scattering mechanisms from ground targets and on its dependency on the radar wavelength. The study was done using the UAVSAR L-band Quad-pol dataset, RADARSAT-2 Quad-pol dataset, ALOS-2 PALSAR-2, ISRO's L&S- Band Airborne SAR (LS-ASAR) Quad-pol and Compact-pol datasets, and the RISAT-1 Compact-pol dataset. Calibration of the airborne PolSAR data was carried to understand the level of polarimetric distortions in the LS-ASAR product that is a precursor mission to the spaceborne Dual-Frequency L&S Band NASA-ISRO Synthetic Aperture Radar (NISAR) mission. It is understood that the crosstalk is the dominant polarimetric distortion, which severely affects the PolSAR datasets compared to the other polarimetric distortions, and it is more for the higher wavelength PolSAR systems. The Quegan, Improved Quegan, and Ainsworth algorithms for crosstalk estimation and minimization was performed for the different Quad-pol datasets and it was found that the Improved Quegan algorithm is suitable for removing crosstalk from datasets having high crosstalk and the Ainsworth algorithm is suitable for removing crosstalk from datasets having low crosstalk. The Freeman method of the polarimetric calibration was implemented for the compact-pol datasets and it was able to considerably minimize the polarimetric distortions. The coherency matrix, scattering matrix, model-based decomposition, polarimetric signatures, and roll invariant parameter-based analysis revealed that all the datasets after polarimetric calibration were showing the correct scattering responses expected from the ground targets.

Keywords: Spaceborne PolSAR; Channel imbalance; Crosstalk; Phase bias; Faraday rotation; CTLR; Quegan algorithm; Improved Quegan algorithm; Ainsworth algorithm; Freeman algorithm; Polarimetric decomposition; NASA-ISRO Synthetic Aperture Radar (NISAR)

* Corresponding author.
E-mail address: shashi@iirs.gov.in (S. Kumar).

https://doi.org/10.1016/j.asr.2021.02.023
0273-1177/

1. Introduction

Active microwave imaging synthetic aperture radar (SAR) remote sensing has many advantages over other remote sensing techniques, not only in land use and land cover classification, but also in modelling to obtain information that is not possible with other techniques (Babu and Kumar, 2019a; Majumdar et al., 2019a; Moreira et al., 2013). Several approaches to various thematic applications have been developed over the past few decades to show the use of SAR backscatter (Ouchi, 2013). The active microwave imaging SAR system has not only the potential to characterize parameters of the objects but also to measure the height of the terrain (Mangla and Kumar, 2014) and vegetation cover (Kumar et al., 2017c), snow parameters retrieval (Awasthi et al., 2021, 2017), movement of the tectonic plates (Chorowicz et al., 1999; McElfresh et al., 2002; Navarro et al., 2009), the lava flow direction of a volcanic eruption (Babu and Kumar, 2019b; Chandni and Kumar, 2020) and subsidence in the earth surface (Asopa et al., 2018) with very high accuracy. The interferometric acquisition of the SAR system provides the ability to retrieve elevation, subsidence, and displacement of the surface (Bamler and Hartl, 1998; Goldstein and Werner, 1998; Massonnet et al., 1993; Rabus et al., 2003; Rosen, 2000). While the normal SAR backscatter showed its sensitivity with forest aboveground biomass (AGB) (Kumar et al., 2012) and soil moisture (Singh et al., 2020), the SAR interferometry gave very good accuracy in the measurement of elevation and displacement (Babu and Kumar, 2019c; Gonnuru and Kumar, 2018; Kumar et al., 2020b). As the utility of SAR remote sensing increased and technology progressed, the scientific community developed data acquisition and processing approaches in view of the importance of PolSAR (Kumar et al., 2020c; Lee and Pottier, 2017; Pottier et al., 2009; Pottier and Ferro-Famil, 2012). Advances in polarimetric synthetic aperture radar (PolSAR) remote sensing are playing an important role in the geophysical and biophysical parameter retrieval of man-made and natural features (Falk et al., 2018). The PolSAR data has shown its advantage over single and dual-polarized SAR data for scattering retrieval in heterogeneous areas. The increase in heterogeneity is a challenging task in the retrieval of backscatter information that is contributed by a wide variety of objects within a small area. The PolSAR scattering-based decomposition models have been demonstrated to retrieve the actual scattering contribution of different objects within a SAR resolution cell (Bhanu Prakash and Kumar, 2021; Shafai and Kumar, 2020). The spaceborne and airborne polarimetric SAR data have been used for different applications that include soil moisture estimation, forest aboveground biomass estimation (Behera et al., 2016; Kumar et al., 2019; Sai Bharadwaj et al., 2015), snow parameter retrieval (Awasthi et al., 2021, 2020; Majumdar et al., 2019b), dielectric characterization (Shukla et al., 2020a), oil spill detection (Chaudhary and Kumar, 2020; Kumar et al., 2016b) ship identification (Grover et al., 2018), etc.... The Polarimetric SAR Tomography (PolTomSAR) and polarimetric SAR Interferometry (PolInSAR) have been developed as emerging techniques to derive forest parameters for canopy height (Asopa and Kumar, 2020; Joshi et al., 2016; Kumar and Joshi, 2017) and aboveground biomass retrieval (Kumar et al., 2017d). The PolInSAR inversion-based approaches use the complex coherence optimization to retrieve forest height (Kumar et al., 2020a) and the PolTomSAR technique is implemented for forest height estimation using a large number of polarimetric acquisitions to create vertical resolution (Joshi and Kumar, 2017; Kumar et al., 2017b, 2017a). The ability of quad-pole and hybrid-pole SAR data has not only been evaluated for the Earth's surface but has also been used for the surface and sub-characterization of planetary bodies (Shukla et al., 2020b; Shukla et al., 2019; Vashishtha and Kumar, 2020). To retrieve PolSAR scattering-based surface properties and parameters for different thematic applications the quality of the data to ensure the accuracy in radar cross-section and scattering measurement is done using radiometric, geometric, and polarimetric calibration techniques (Fore et al., 2015; Shimada et al., 2009; Van Zyl and Kim, 2011). "Calibration of SAR is meant to formulate the image pixel intensity and the normalized radar cross-section (NRCS) in deploying the corner reflectors or the active radar calibrators, whose radar cross-sections and locations are well known" (Shimada, 1996). To ensure image quality, the spaceborne SAR system's performance needs to be monitored regularly through internal and external calibration approaches (Srivastava et al., 2007, 2003, 2001, 1999, 1997, 1996). The radiometric and geometric calibration ensures the accuracy in backscatter cross-section and location of a point target in single-, dual- and quad-pol SAR data (Freeman and Curlander, 1989; Mohr and Madsen, 2001; Schubert et al., 2015; Ulander, 1996). The geometric location accuracy, which is also known as Absolute Location Error (ALE), is the difference between the actual position of a target on the ground and the image derived location of the same target in an SAR image (Balss et al., 2018). The characteristic of the SAR system on well-calibrated measures of backscatter intensity, or the power of scattered electromagnetic waves, is called radiometric calibration (Woodhouse, 2006). Nowadays radiometric and geometric calibration is not a tough task if a sufficient number of SAR acquisitions are available over the locations of active and passive calibrators (Freeman et al., 1990; Fujita et al., 1998; Shi et al., 2020; Sun et al., 2017; Touzi et al., 2013; Wang et al., 2019). The polarimetric calibration is essentially required to ensure the polarimetric quality of a fully polarimetric quad-pol and hybrid/compact-pol SAR data (Babu et al., 2019a,b; Chen and Quegan, 2011; Reimann et al., 2017; Tan and Hong, 2015, 2016; Zhang et al., 2017). Any ambiguity in PolSAR data due to polarimetric distortions would affect the scattering information of different objects that will be retrieved through polarimetric decomposition mod-

elling (Babu et al., 2019a,b; Babu et al., 2020). Several studies have been carried to explore the effect of polarimetric distortions in PolSAR-based decomposition modelling and all the studies have strongly suggested an accurate polarimetric calibration of airborne and spaceborne SAR data for scattering-based characterization of manmade and natural features (Babu, 2019; Maiti, 2019; Maiti et al., 2021).

The fully polarimetric SAR data of a spaceborne SAR system mainly suffers from three types of polarimetric distortions, which affect the quality of the data for scattering-based characterization of manmade and natural features. The three polarimetric distortions of a spaceborne SAR are crosstalk, channel imbalance, and Faraday rotation. In a fully polarimetric SAR system, a horizontally polarised electromagnetic wave should not register a signal in the vertical channel, and vice versa (Woodhouse, 2006). The crosstalk is a cross-polarised leakage, which occurs when some amount of vertically polarised signal is mixed with horizontally polarised signals or vice versa. The crosstalk occurs between the co-polarized and cross-polarized channels of a PolSAR dataset due to the non-ideal behaviour of transmit-receive modules (TRMs) during transmission and reception of the microwave signals (Chang et al., 2018). The spacing, width, and type of the horizontal and vertical transmission and receiver channels are mainly responsible for crosstalk. As per the science application's quality requirements of the PolSAR datasets, the crosstalk should be less than −30 dB (Freeman et al., 1990) for Geophysical parameter inversion and multi-temporal studies. The channel imbalance and phase bias occur between the co-polarized and cross-polarized channels are due to the difference in gain of power amplifiers (PA) between horizontal and vertical polarizations of the same TRM and different TRMs, the difference in sidelobe suppressing capacity of Low Noise Amplifiers (LNA) and difference in attenuator behaviour between horizontal and vertical polarizations. Faraday rotation error occurs when a linearly polarized EM wave propagates through the Earth's Ionosphere. The charged ions present at the Ionosphere changes the polarization plane of the linearly polarized EM wave when it traverses through it. Faraday rotation error is affected only for spaceborne SAR systems (Chang et al., 2018). For a Quad-pol SAR system, both transmission and reception are done using linearly polarized EM waves, so the Faraday rotation error is affected two times and is more dominant for low-frequency SAR systems operating in L-band and P-band. In a CTLR SAR system, since transmission is done using circularly polarized EM waves, the Faraday rotation is affected only during signal reception.

To measure accurate geophysical parameters from backscatter-based measurements, SAR data must be free of any distortion and this could be achieved by internal and external calibration schemes (Carter et al., 1997; Freeman, 1992; Seifert et al., 1996). Several studies have been performed to reduce the polarimetric distortion of a SAR system through an internal calibration scheme in which the variation in the gain of the system is measured using an internal calibration loop (Gong et al., 2017; Liang et al., 2020; Schwerdt et al., 2017; Wang et al., 2009). Mainly three types of calibrators are used in external calibration to measure polarimetric distortion in a SAR system and these are polarimetric active radar calibrator (PARC) (Brunfeldt and Ulaby, 1984; Freeman et al., 1990; Fujita et al., 1998; Lenz et al., 2006; Li et al., 2012; Sarabandi et al., 1992a; Shimada et al., 1999), corner reflectors as passive receivers (Ferrer et al., 2011; Liang et al., 2020; Sheen et al., 1992; Shimada et al., 2009; Sun et al., 2017), and homogenously distributed natural targets (Fore et al., 2015; Liang et al., 2020; Sarabandi et al., 1995, 1992b).

Spaceborne or airborne polarimetric SAR (PolSAR) systems are capable of providing accurate scattering of an object with the help of different polarimetric combinations for the targeted area. A SAR system is operated in dual-pol, quad-pol, or compact/hybrid-pol modes of the data acquisition. In a Dual-polarized SAR system, a Horizontal/Vertical polarized electromagnetic wave is transmitted and then both Horizontal and vertically polarized EM waves are received simultaneously. So from a dual-pol SAR system, two channels are obtained viz. Horizontal polarization transmitted: Horizontal polarization received (HH) and Horizontal polarization transmitted: Vertical polarization received (HV) or Vertical polarization transmitted: Horizontal polarization received (VH) and Vertical polarization transmitted: Vertical polarization received (VV) (Velotto et al., 2016). In a Quad-polarized SAR system, a horizontally polarized EM wave is transmitted and the receiver receives both horizontal and vertical polarized EM waves backscattered by the ground targets simultaneously. After receiving all the backscattered EM waves from near range to far range, the vertically polarized EM wave is transmitted and the horizontal and vertical polarized backscattered EM waves are received (Fig. 1). So from a quad-pol SAR system, 4 channels can be obtained viz. Horizontal polarization transmitted: Horizontal polarization received (HH), Horizontal polarization transmitted: Vertical polarization received (HV), Vertical polarization transmitted: Horizontal polarization received (VH) and Vertical polarization transmitted: Vertical polarization received (VV) (Livingstone et al., 2015). The circular and linear receive mode of the hybrid polarimetric SAR system transmits only one polarization to generate dual-pol SAR data (Fig. 2). The hybrid-pol SAR systems are capable to increase the swath width without compromising the spatial resolution to take an advantage of polarimetric scattering characterization of the objects (Jayasri et al., 2018; Raney, 2007; Touzi, 2009). A polarimetric SAR data must be free of distortions to conduct quantitative analysis using PolSAR data, time series analysis and to compare results between different sensors. The development of efficient polarimetric calibration techniques for maintaining the science quality requirements of the PolSAR datasets is very

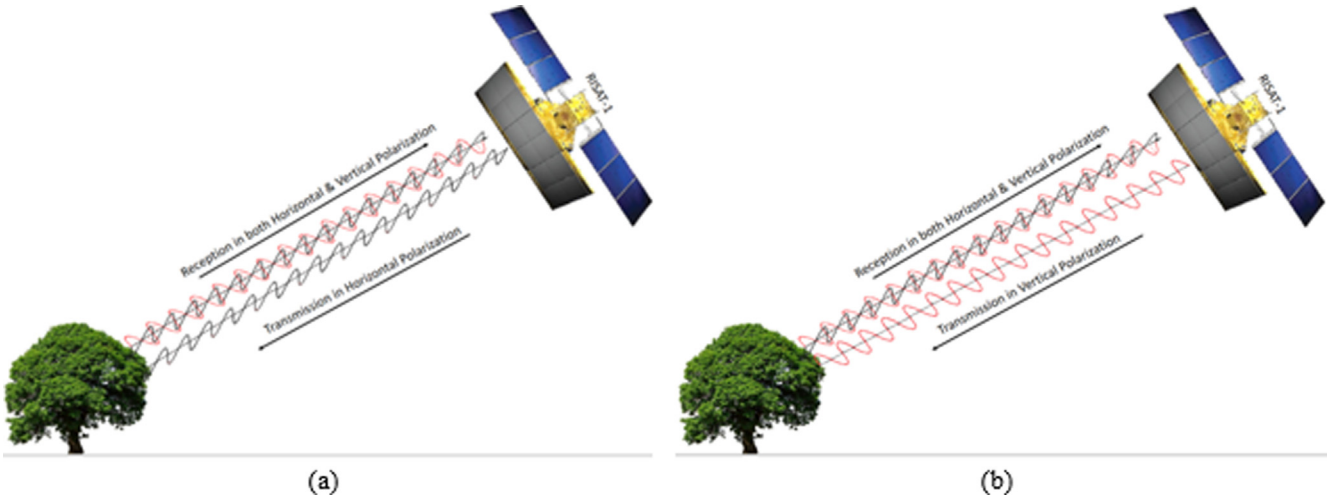

Fig. 1. Quad-pol SAR Scheme; (a) Horizontal transmit & Horizontal and Vertical receive; (b) Vertical transmit & Horizontal and Vertical receive.

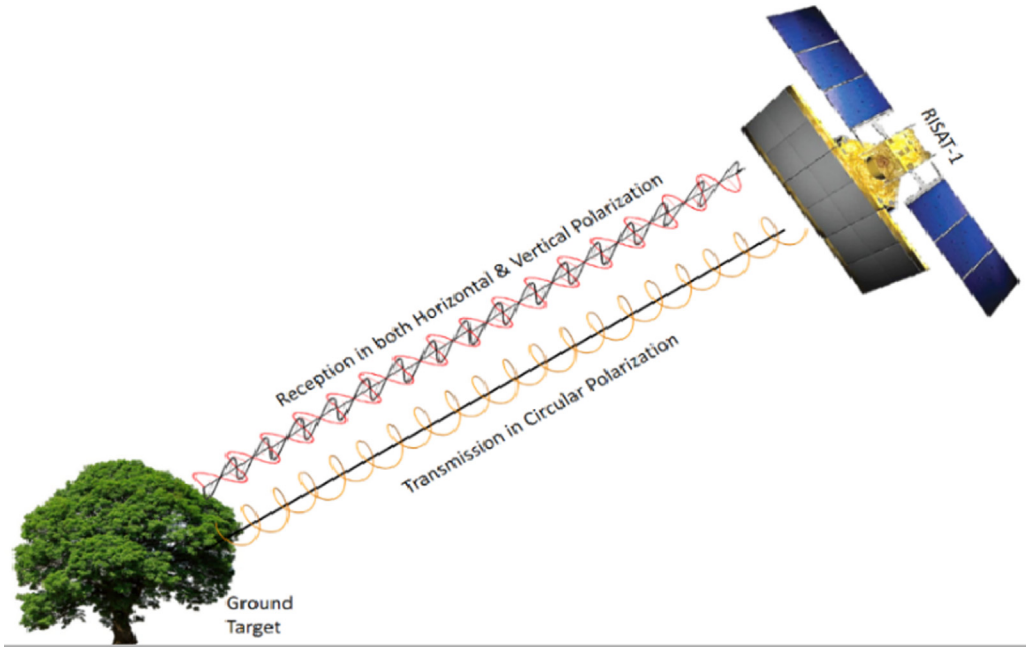

Fig. 2. CTLR SAR scheme- Circular transmit: Horizontal and Vertical receive.

relevant to the Indian Remote Sensing community as well as the global community in the context of the upcoming spaceborne SAR missions. PolSAR calibration will be a mandatory requirement for upcoming global SAR missions; some of the most important missions are dual-frequency L- and S-band NASA-ISRO Synthetic Aperture Radar (NISAR) mission (Chapman et al., 2019; Falk et al., 2018; Kellogg et al., 2020), the European Space Agency's (ESA's) P-band Biomass mission (Labrière et al., 2018; Toan et al., 2018), Tandem-L mission (Moreira et al., 2018; Tridon et al., 2018) of German Aerospace Center (DLR) and Radar Imaging Satellite (RISAT) missions of Indian Space Research Organisation (ISRO).

This study evaluates the level of polarimetric distortions in fully polarimetric quad-pol and dual-polarimetric hybrid/compact-pol datasets of multiple frequencies and different methods of polarimetric calibration were analyzed to understand their potential in minimizing these polarimetric distortions. The PolSAR calibration was performed on multifrequency SAR data that includes; C-band fully polarimetric quad-pol SAR data of RADARSAT-2, hybrid-pol SAR data of Radar Imaging Satellite-1 (RISAT-1), Phased Array type L-band Synthetic Aperture Radar (PALSAR-2) data of Advanced Land Observing Satellite-2 (ALOS-2), L&S Band Airborne SAR (LS-ASAR) data that was acquired under NISAR L&S Airborne SAR Research Announcement (RA) of Indian Space Research Organisation (ISRO) and L-band SAR data of Uninhabited Aerial Vehicle Synthetic Aperture Radar (UAVSAR). Special emphasis was given to analyze the

impact of the polarimetric distortions on accurate ground target characterization before and after polarimetric calibration. The polarimetric calibration algorithms were tested on multifrequency airborne and spaceborne SAR data using Polarimetric SAR Calibration and Processing Tool v1.0 (PSCP v1.0) (Kumar et al., 2020c), which was developed at Indian Institute of Remote Sensing (IIRS), ISRO, Dehradun under the Technology Development Programme (TDP) and NISAR L&S Airborne SAR Research Announcement (RA) of Indian Space Research Organisation (ISRO).

2. Study area and dataset

The polarimetric calibration was performed to the multifrequency spaceborne and airborne SAR data of four different locations. Fig. 3 illustrates the locations where corner reflectors were deployed by the respective space agencies for polarimetric calibration of quad-pol SAR data. The locations of the corner reflectors are shown in the Global Land Cover product at 100 m spatial resolution of Copernicus Global Land service (CGLS) (Buchhorn et al., 2020b, 2020a). The PROBA-V product-based near real-time epoch 2019 global land cover has 23 discrete classes as visible in Fig. 3 and the details of discrete classes are given in the product user manual (Buchhorn et al., 2020b). The boundary of India is shown in saffron color where corner reflectors were deployed at two different locations. Four corner reflectors were deployed in Dehradun, Uttarakhand India by the PolSAR calibration team of the Indian Institute of Remote Sensing (IIRS), Indian Space Research Organisation (ISRO) for calibration of spaceborne C-band RADARSAT-2 data. The location of all the four corner reflectors that were used in PolSAR calibration of RADARSAT-2 data in Dehradun, India is shown in Fig. 4a.

Freeman-Durden decomposition (Freeman and Durden, 1998) based false colour composite image of the RADARSAT-2 data over Google Earth is shown in Fig. 4a in which surface scattering, double-bounce scattering and volume scattering elements are represented in blue, red and green colour respectively. Black coloured text CR01, CR02, CR03 and CR04 are the abbreviation of corner reflector to show their location in Fig. 4a.

Trihedral and dihedral corner reflectors were deployed by the SAR CalVal team of Space Applications Centre (SAC), ISRO, Ahmedabad at Desalpar, Rann of Kutchh, Gujarat, India for calibration of C-band spaceborne Radar Imaging Satellite-1 (RISAT-1) and L-&S-band airborne SAR data (Sharma et al., 2017). The three different types of corner reflectors include 90 cm side length triangular trihedral, 60 cm side length square trihedral, and 1.2 m side length dihedral corner reflectors. Three different types of corner reflectors were used for calibration of SAR data and their dimensions were triangular trihedral with a side length of 90 cm, square trihedral with a side length of 60 cm, and dihedral corner reflector with a side length of 1.2 m (Sharma et al., 2017). The location of corner reflectors in Rann of Kutchh is shown in the yellow-colored triangular shape in Cloude's three-component compact decomposition model-based color composite image.

Corner reflectors were placed on a perfectly smooth surface in Rann of Kutch, so it is expected that the dominance of surface scattering elements will be observed, but due to polarimetric distortions in the RISAT-1 hybrid / compact polarimetric SAR data, it could be seen that the underesti-

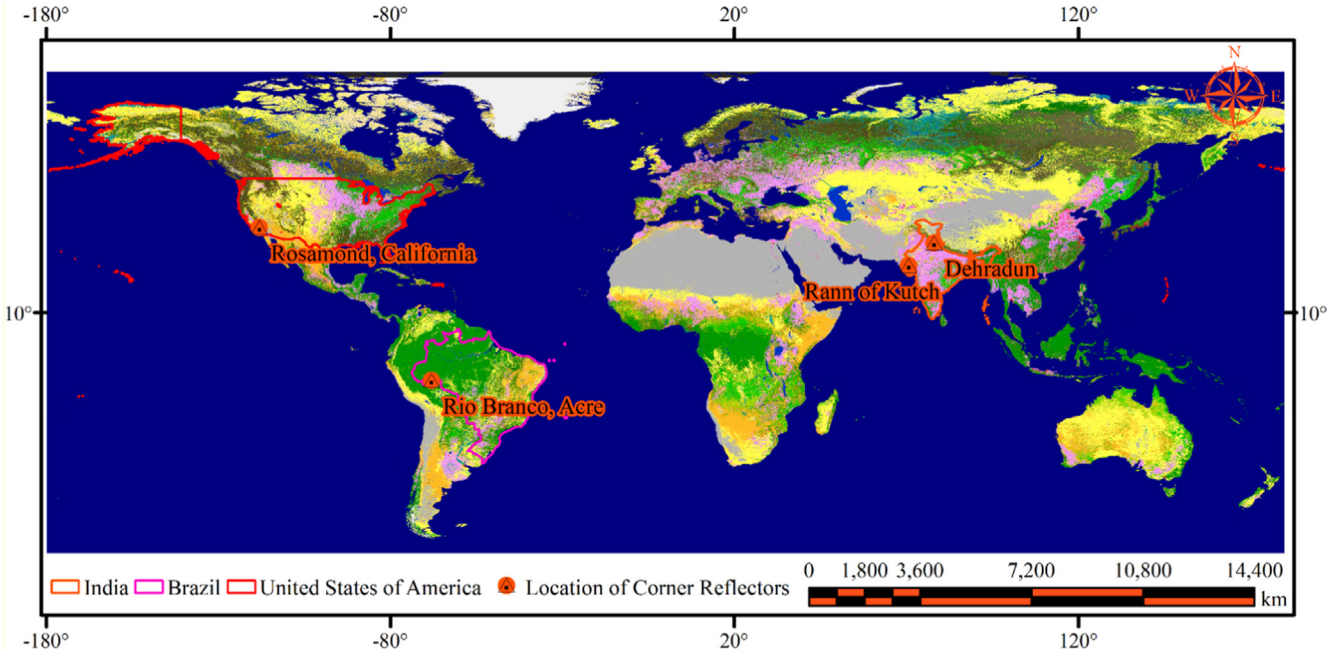

Fig. 3. Location of calibration sites of airborne and spaceborne multifrequency SAR data.

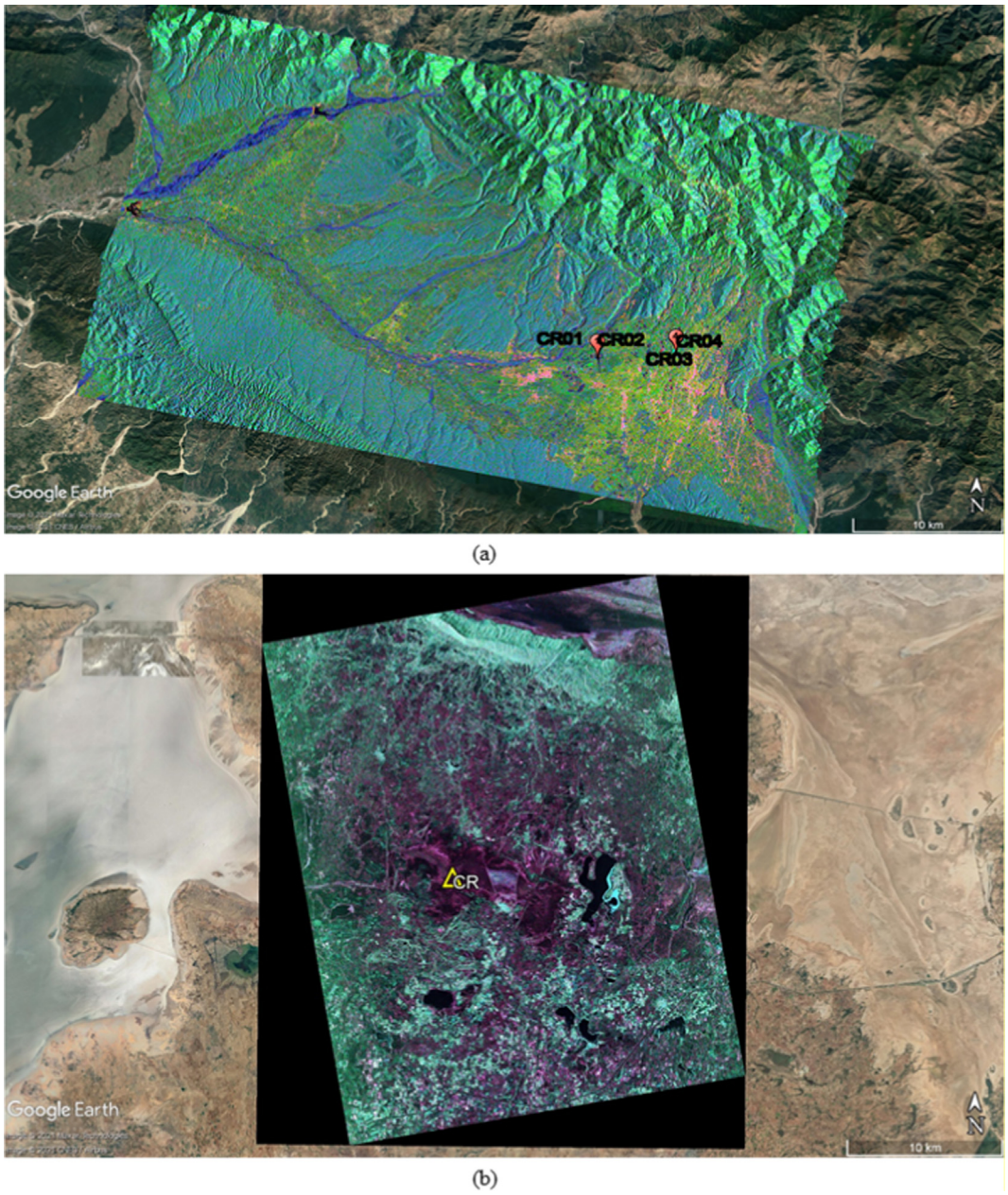

Fig. 4. Location of corner reflectors in (a) Freeman-Durden decomposition-based false-color composite of RADARSAT-2 data for Dehradun, India (b) Cloude's three-component decomposition-based false-color composite of RISAT-1 data for Desalpar, Rann of Kutch, India.

mation in the surface scattering element (blue color) and overestimation in the double bounce scattering (red color) is obtained for smooth surfaces.

The boundary (Upadhyay, 2021a) of Brazil is shown in Ginger Pink color, and the location of the reflectors is highlighted by a black triangle in the saffron circle in Fig. 3. These reflectors were established and deployed by the Japan Aerospace Exploration Agency (JAXA) for calibration of SAR data (IDEAS SAR Team, 2009; Moriyama, 2015). A 3 m length triangular corner reflector (Rao and Kumar, 2017) was used in this study for PolSAR calibration of the Phased Array type L-band Synthetic Aperture Radar (PALSAR-2) data of Advanced Land Observing Satellite-2 (ALOS-2). The location of the corner reflector is shown in Fig. 5a in the orange color triangle in the Freeman-Durden decomposition-based false-color composite image of quad-pol SAR data of ALOS-2 PALSAR-2 for Rio Branco, Acre, Brazil. The dense forest cover is represented in green color to show the dominance of volume scattering and smooth surfaces are highlighted in blue color, which shows the dominance of surface scattering.

The Rosamond Corner Reflector Array (RCRA) consists of trihedral corner reflectors (CRs) in California, United States of America (USA) (Muellerschoen, 2020). The boundary map of the USA which was downloaded from

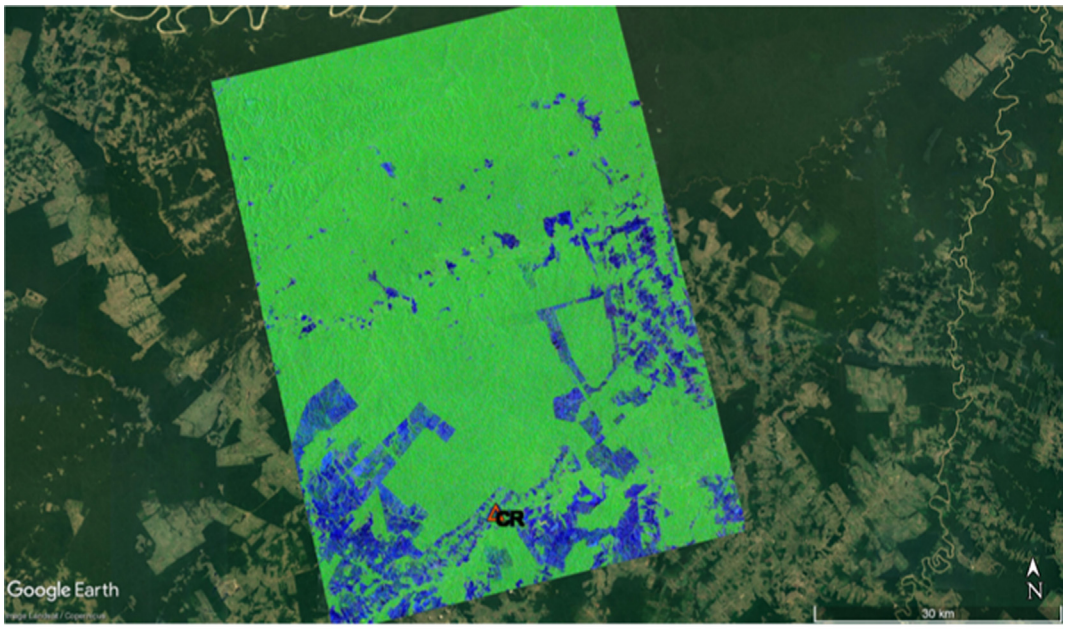

(a)

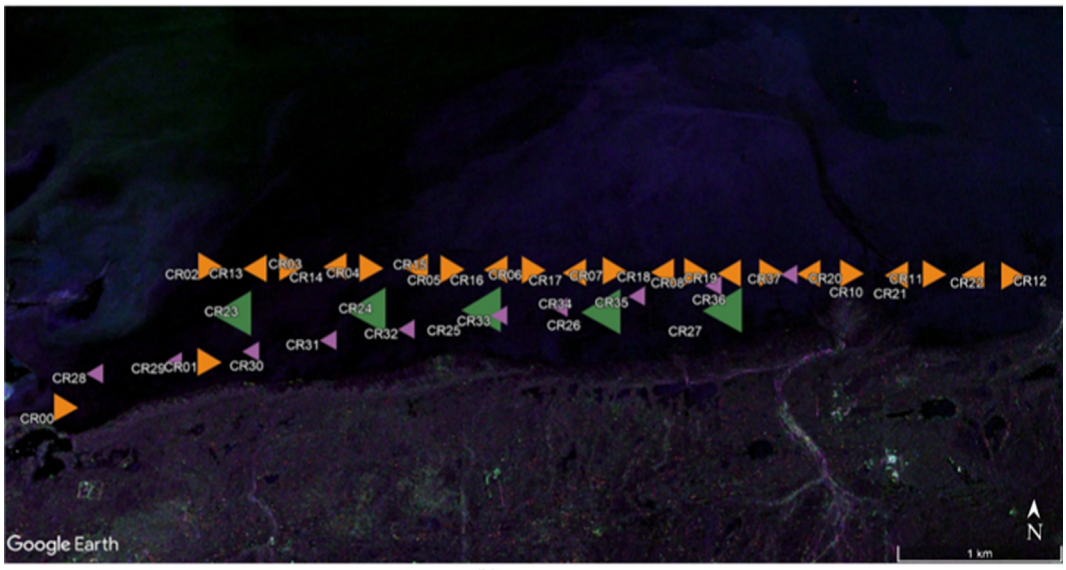

(b)

Fig. 5. Location of corner reflectors in (a) Freeman-Durden decomposition-based false-color composite of ALOS-2 PALSAR-2 data for Rio Branco, Acre, Brazil (b) Pauli's decomposition-based false-color composite of UAVSAR data for the Rosamond Corner Reflector Array (RCRA), California, United States of America (USA).

IGISMAP (Upadhyay, 2021b) is shown in red color in Fig. 3. The Rosamond Calibration Array (RCA) consists of twenty-three 2.4-meter CRs, five 4.8-meter CRs and ten 0.7-meter CRs. An overlay of Pauli RGB image of L-band UAVSAR data over Google Earth is shown in Fig. 5b. Corner reflectors of different sizes in RCRA are shown in different colors in Fig. 5b. Twenty-three corner reflectors of 2.4-meter side length are shown in orange color triangles, five corner reflectors of 4.8-meter side length are shown in green color triangles, and ten corner reflectors of 0.7-meter side length are shown in pink color triangles.

Fully polarimetric C-band quad-pol SAR data of RADARSAT-2 were acquired over Dehradun, India on 18 February 2019 and 14 March 2019. Right Circular Transmit and Linear Receive (CTLR) Hybrid Polarimetric Dual-pol SAR Data of Radar Imaging Satellite (RISAT-1) was acquired on 15 February 2016. The RISAT-1 data was acquired in Fine Resolution Stripmap mode-1 (FRS-1) to get RH and RV Hybrid Polarimetric Dual-pol SAR Data. As a precursor to the development of dual-frequency spaceborne SAR, an airborne SAR in L& S-band was planned with similar specifications of the NISAR mission (Das et al., 2019; Space Applications Centre, 2016) The

L-&S-band airborne SAR data were acquired over Desalpar, Rann of Kutch in Hybrid Polarimetric Dual-pol and fully polarimetric quad-pol modes. The detailed information of multifrequency airborne and spaceborne SAR data is shown in Table 1. The single look complex (SLC) data of hybrid/compact-pol and fully polarimetric quad-pol data were used to estimate the polarimetric distortions in the SAR data.

3. Methodology

3.1. Deployment of corner reflectors

At all the four locations, different teams and space agencies deployed corner reflectors. The Japan Aerospace Exploration Agency (JAXA) deployed CR in Rio Branco, Acre, Brazil (IDEAS SAR Team, 2009; Moriyama, 2015), NASA's Jet Propulsion Laboratory deployed CRs in Rosamond, California, USA for UAVSAR calibration (Muellerschoen, 2020). Corner reflectors in Rann of Kutch are deployed and maintained by SAR CalVal team of Space Applications Centre (SAC). Out of all the four sites, the calibration team of Indian Institute of Remote Sensing (IIRS), ISRO, Dehradun did the field campaign with 4 corner reflectors in Dehradun, India for the calibration of spaceborne C-band SAR data of the RADARSAT-2 satellite. The trihedral triangular corner reflectors were used in the PolSAR calibration of RADARSAT-2 data for Dehradun, India. Trihedral corner reflectors (square or triangular) are widely used and the most practical devices, which are used as external calibrators to calibrate SAR data (Schubert et al., 2017). The corner reflectors with 1 m side lengths were manufactured as per the specification mentioned in the report of the Australian Geophysical Observing System (Garthwaite et al., 2015).

3.1.1. Design of corner reflector for deployment in Dehradun

The parts of the Triangular trihedral corner reflector and its deployment is explained here. The main parts of the corner reflector are: Triangular base frame, Base T frame, centre frame, screwed rod and triangular panels.

The base triangular frame with the base T frame fitted on top on it is shown in the Fig. 6a. The base triangular frame is used to rigidly mount the corner reflector to the ground. This frame is mounted to the ground by hammering long screws or iron rods. All the other parts of the corner reflector are fitted on top of it. The base T frame is mounted on top of the triangular base frame. The centre frame and screwed rods are attached to the base T frame. The base T frame is mounted to the triangular base frame using a spindle and the base T frame can be rotated 360 degrees on top of the triangular base frame for orienting the corner reflector to correct azimuth direction of the satellite pass. Two screws are used to stop the rotation of the base T frame after orienting it to the correct azimuth direction. The centre frame (Fig. 6c) is mounted on top of the base T frame (Fig. 6a). The three triangular reflect-

Table 1
Detailed description of multifrequency airborne and spaceborne SAR data.

SAR System	L & S Airborne SAR				UAVSAR	ALOS-2 PALSAR-2	RADARSAT-2		RISAT-1
Sensor	Airborne					Spaceborne			
Date of acquisition	24 June 2017				11 Feb 2016	08 August 2014	18 Feb 2019	14 March 2019	15 Feb 2016
Product ID	L_S_Joint_CP_ID37_Line1_Run2_24june2017		L_S_Joint_CP_ID37_Line1_Run1_24june2017		Rosamd_35012_16002_001_160211_L090_04	ALOS2011247000-140808	PDS_07004050		PDS_07141830
Polarimetric Mode	Quad-pol		Compact-pol		Quad-pol	Quad-pol	Quad-pol		Compact-pol
Polarisations	(HH+HV+VH+VV)		(RH+RV)		(HH+HV+VH+VV)				(RH+RV)
Band	L-band	S-band	L-band	S-band	L-band	L-band	C-band		C-band
Frequency	1250 MHz	3200 MHz	1250 MHz	3200 MHz	1257.50 MHz	1236.499 MHz	5404.999 MHz		5350 MHz
Wavelength	23.98 cm	9.36 cm	23.98 cm	9.36 cm	23.84 cm	24.24 cm	5.54 cm		5.60 cm
Range resolution (Meters)	1.8 m		1.8 m		1.6 m	2.86 m	5.2 m		2.34 m
Azimuth resolution(Meters)	2.05 m		1.96 m		0.6 m	2.78 m	7.6 m		3.33 m
Look direction	Left		Left		Left	Right	Right		Right
Look angle range	15.64° - 48.06°		15.57°-48.05°		21.32° - 66.17°	25.615° - 29.76°	34.78° - 37.63°		31.87°-34.12°
Platform Altitude (Kilometers)	8.528 km		8.531 km		12.495 km	628.00 km	795.10 km		543.210 km

Fig. 6. Parts of the corner reflector (a) base T frame of the Triangular Trihedral corner reflector (b) triangular reflecting panels (c) Center Frame (d) Screwed rod (e) Deployment of the Triangular Trihedral corner reflector.

ing plates (Fig. 6b) of the trihedral corner reflectors are mounted on the centre frame. The centre frame after mounting the triangular panels generates the trihedral geometry which causes the triple bounce scattering mechanism of the incident EM wave from the radar and directs its back to the radar antenna. The screwed rod (Fig. 6d) holds firmly the centre frame and the base T frame. The main purpose of this rod is to tilt the center frame and the triangular panels without disturbing the base T frame and the triangular base frame. The tilting of the triangular panels is required to adjust its elevation angle to allow the EM wave from the radar to the incident at the bore sight of the corner reflector. This ensures the maximum RCS from the corner reflector. Fig. 6e shows the deployment of the corner reflector and the attachment of the different corner reflector parts to each other.

3.1.2 Field campaign at Dehradun for the deployment of triangular trihedral corner reflectors

Two field campaigns were organized by Indian Institute of Remote Sensing (IIRS), ISRO, Dehradun for deploying the triangular trihedral corner reflectors at the FRI campus and SOI ground. The first field campaign was done on 17th February 2019 and the second field campaign was done on 13th March 2019.

The azimuth angle and incidence angle of the satellite pass is required for properly deploying the corner reflectors in the line of sight with the radar antenna to obtain the maximum Radar Cross Section (RCS) from the Corner reflector. For obtaining the maximum RCS, the relative incidence angle between the Radar beam and the Triangular trihedral corner reflectors should be 54.74 degrees, so the elevation angle of the corner reflectors should be adjusted to maintain this relative incidence angle. The relationship between the incidence angle, elevation angle and the relative incidence angle is as follows:

$$Elevation\ \ angle = 54.74 - Incidence\ \ angle$$

elevation angles required for deploying the Triangular trihedral corner reflectors for the specific satellite pass is shown in Table 2. Since repeat pass datasets were acquired for both the field campaigns, the corner reflectors were deployed with the same parameters.

The triangular trihedral corner reflectors deployed at Survey of India (SOI), Dehradun and Forest Research Institute (FRI), Dehradun campuses. Total four corner reflectors with one-meter inner side arm length are deployed at both the locations with the azimuth angle and elevation angle shown in Table 2. The azimuth angle of the corner reflectors from the magnetic north direction is accurately measured using both digital and analogue compass. The elevation angle of the corner reflectors from the horizontal plane is accurately measured using a digital inclinometer (Fig. 7a, b). The precise position of corner reflectors were measured with the Trimble R7 GNSS System. The position measurement with high-accuracy Trimble R7 GNSS System was measured during the deployment of corner reflectors as shown in Fig. 7c. The coordinates of all the four corner reflectors in the display unit of the Trimble R7 GNSS System is shown in Fig. 7d. Fig. 7e shows a photograph of the PolSAR calibration team that was taken during the deployment of a corner reflector at one location.

3.2. Methodology for polarimetric calibration of quad-pol datasets

The methodological flow diagram used in PolSAR calibration of airborne and spaceborne SAR quad-pol data to minimize polarimetric distortions is shown in Fig. 8. Looking at the polarimetric decomposition image (Fig. 4a and Fig. 5a), it appears that both ALOS-2 PALSAR-2 and RADARSAT-2 data are given to the user after PolSAR calibration, yet the level of distortion is estimated in this study.

The quad-pol datasets were first radiometrically calibrated using the absolute calibration constant derived from the corner reflectors. After the radiometric calibration, the next step is to estimate and correct the channel imbalances and phase bias. This process is carried out using both the corner reflectors and homogeneously distributed targets present in the study area. Once the dataset is free from channel imbalance and phase bias errors the crosstalk between the different polarization channels can be estimated. The Quegan, Improved Quegan, and Ainsworth methods of crosstalk estimation were implemented and the crosstalk values were estimated and corrected. After removing the crosstalk, the dataset is free from all polarimetric distortions. For spaceborne Quad-pol datasets, after crosstalk correction one additional step is done to estimate and remove the Faraday rotation error.

The initial step of the PolSAR calibration involves the estimation of the absolute calibration constant A using equation (1) (Fore et al., 2015):

$$10log_{10}\left[\frac{\sigma_{cr}}{(O_{hh}O^{*}_{hh})}\right] = -10log_{10}A^{2} \tag{1}$$

Equation (1) is used to estimate absolute calibration constant (A) with the help of theoretical radar cross-section (RCS) of the corner reflector and the maximum complex backscatter value of HH channel (O_{hh}) and its complex conjugate (O^{*}_{hh}).

After estimating the absolute calibration factor, the channel imbalances and phase bias need to be estimated. The co-channel imbalance f is estimated using the corner reflectors as follows (Chang et al., 2018; Fore et al., 2015):

$$f = \left[\frac{(O_{vv}O^{*}_{vv})}{(O_{hh}O^{*}_{hh})}\right]^{0.25} \tag{2}$$

Table 2
Azimuth angle and Elevation angles required for the corner reflectors deployed at Dehradun for RADARSAT-2 FQ16W pass.

Location	Azimuth angle	Incidence angle	Elevation angle
Forest Research Institute (FRI)	100.7	35.29	19.45
Survey of India (SOI)	100.7	35.63	19.11

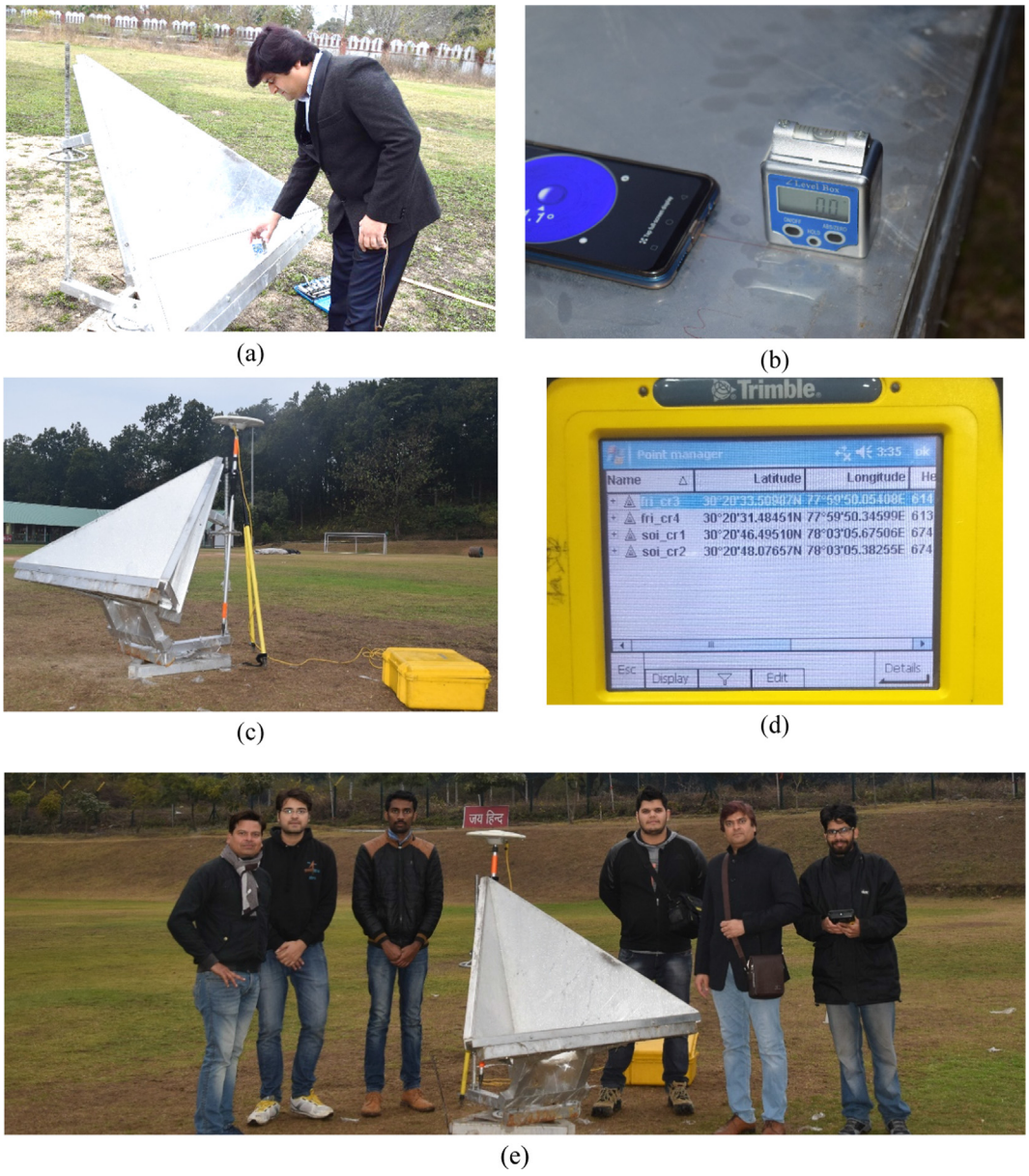

Fig. 7. (a) Elevation angle measurement using inclinometer (b) Reading of inclinometer at zero inclination (c) Position measurement corner reflector Trimble R7 GNSS System (d) Display unit of the Trimble R7 GNSS System (e) Members of PolSAR calibration team with field-deployed corner reflector.

To measure the co-channel imbalance (f) maximum backscatter values (O_{hh}, O_{vv}) of co-pol channels (HH and VV) and their complex conjugates ($O^*_{hh,}O^*_{vv}$) are measured from the uncalibrated SAR data.

The cross-channel imbalance g is estimated using the homogeneously distributed targets like vegetation or bare soil as follows (Chang et al., 2018; Fore et al., 2015):

$$g = \left[\frac{\langle |O_{hv}|^2 \rangle}{\langle |O_{vh}|^2 \rangle}\right]^{0.25} \tag{3}$$

where, O_{hv} and $O_{hv}$are the maximum complex backscatter values of HV and VH channels of the uncalibrated SAR data. The <> symbol indicates the averaging operation over a large number of pixels.

The phase bias occurred during signal transmission is represented by ϕ_t and the phase bias occurred during signal reception is represented by ϕ_r. ϕ_t and $\phi_r$cannot be estimated directly and it needs to be estimated indirectly. The term $(\phi_t + \phi_r)$ can be directly estimated using corner reflector as follows (Chang et al., 2018; Fore et al., 2015):

$$(\phi_t + \phi_r) = \arg\left(O_{vv}O^*_{hh}\right) \tag{4}$$

The term $(\phi_t - \phi_r)$ can be estimated by considering the reciprocity condition ($O_{hv} = O_{vh}$) as follows (Chang et al., 2018; Fore et al., 2015):

$$(\phi_t - \phi_r) = \arg\left(\langle O_{hv}O^*_{vh}\rangle\right) \tag{5}$$

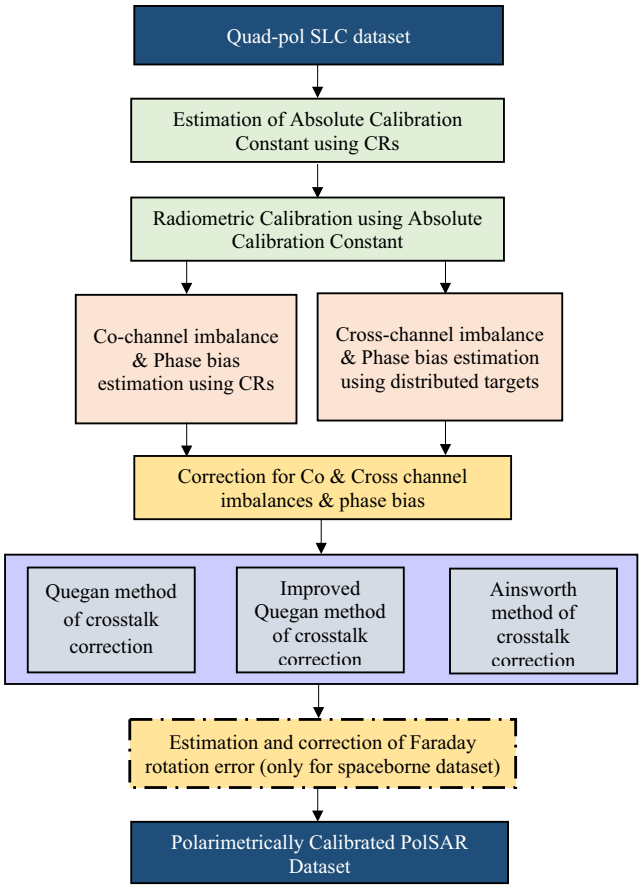

Fig. 8. Methodology flowchart for polarimetric calibration of Quad-pol datasets.

The polarimetric distortion matrix introduced in all three methods were used to relate the intermediate scattering matrix $\left[S^{'}\right]$ free from channel imbalances and crosstalk to the theoretical scattering matrix $[S]$ (Fore et al., 2015).

$$\begin{bmatrix} S'_{hh} \\ S'_{hv} \\ S'_{vh} \\ S'_{vv} \end{bmatrix} = A \begin{bmatrix} 1 & w & v & vw \\ u & 1 & uv & v \\ z & wz & 1 & w \\ uz & z & u & 1 \end{bmatrix} \begin{bmatrix} ak^2 & 0 & 0 & 0 \\ 0 & ak & 0 & 0 \\ 0 & 0 & k & 0 \\ 0 & 0 & 0 & 1 \end{bmatrix} \begin{bmatrix} S_{hh} \\ S_{hv} \\ S_{vh} \\ S_{vv} \end{bmatrix} + \begin{bmatrix} N_{hh} \\ N_{hv} \\ N_{vh} \\ N_{vv} \end{bmatrix} \tag{6}$$

In the equation, 6 (u, v, w, z) are the crosstalk parameters,$[N]$ is the noise matrix and *kanda* are the co-channel and cross-channel imbalances. Since the dataset is already absolutely calibrated and channel imbalances have removed, the values of $A = 1$ and $= 1/\sqrt{a}$. So the equation (6) can be modified as follows:

$$\begin{bmatrix} S'_{hh} \\ S'_{hv} \\ S'_{vh} \\ S'_{vv} \end{bmatrix} = D \begin{bmatrix} S_{hh} \\ S_{hv} \\ S_{vh} \\ S_{vv} \end{bmatrix} + \begin{bmatrix} N_{hh} \\ N_{hv} \\ N_{vh} \\ N_{vv} \end{bmatrix} \tag{7}$$

where D is the distortion matrix, which can be estimated as follows:

$$D = \begin{bmatrix} 1 & w/\sqrt{a} & v/\sqrt{a} & vw \\ u & \sqrt{a} & uv/\sqrt{a} & v \\ z & wz/\sqrt{a} & 1/\sqrt{a} & w \\ uz & z/\sqrt{a} & u/\sqrt{a} & 1 \end{bmatrix} \tag{8}$$

Finally, matrix inversion is done to estimate the theoretical scattering matrix $[S]$ from the intermediate scattering matrix $\left[S^{'}\right]$ as the solution is as follows:

$$\begin{bmatrix} S_{hh} \\ S_{hv} \\ S_{vh} \\ S_{vv} \end{bmatrix} = \sum \left[\begin{bmatrix} S'_{hh} \\ S'_{hv} \\ S'_{vh} \\ S'_{vv} \end{bmatrix} - \begin{bmatrix} N_{hh} \\ N_{hv} \\ N_{vh} \\ N_{vv} \end{bmatrix} \right] \tag{9}$$

where $\sum$ is the calibration matrix estimated as follows:

$$\sum = \begin{bmatrix} 1 & -w & -v & vw \\ -u/\sqrt{a} & 1/\sqrt{a} & uv/\sqrt{a} & -v/\sqrt{a} \\ -z/\sqrt{a} & wz/\sqrt{a} & \sqrt{a} & -w\sqrt{a} \\ uz & -z & -u & 1 \end{bmatrix} \frac{1}{(uw-1)(vz-1)} \tag{10}$$

Quegan, Improved Quegan, and Ainsworth algorithms were used to estimate the u, v, w, z, and a parameters and they differ each other in the way they estimate these (Ainsworth et al., 2006; Fore et al., 2015; Kimura et al., 2004; Quegan, 1994).

After estimating, the complex crosstalk parameters the values are substituted in equation (10) and then equation (9) is evaluated to derive the scattering matrix $[S]$ free from crosstalk distortions. After including the Faraday rotation error, the distortion matrix is represented by the equation (11) (Li et al., 2018; Shimada, 2019):

$$\begin{bmatrix} M_{HH} & M_{HV} \\ M_{VH} & M_{VV} \end{bmatrix} = \begin{bmatrix} cos\Omega & sin\Omega \\ -sin\Omega & cos\Omega \end{bmatrix} \begin{bmatrix} S_{HH} & S_{HV} \\ S_{VH} & S_{VV} \end{bmatrix} \begin{bmatrix} cos\Omega & sin\Omega \\ -sin\Omega & cos\Omega \end{bmatrix} \tag{11}$$

In equation (11) scattering matrix free from Faraday rotation error is represented by $[S]$ and $[M]$ represents the scattering matrix with the error. The Faraday rotation angle is shown by Ω. Estimation of Faraday rotation for a CTLR SAR system is shown in equation (12)(Bickel and Bates, 1965; Shimada, 2019).

$$\begin{bmatrix} M_{LL} & M_{LR} \\ M_{RL} & M_{RR} \end{bmatrix} = \begin{bmatrix} 1 & j \\ j & 1 \end{bmatrix} \begin{bmatrix} M_{HH} & M_{HV} \\ M_{VH} & M_{VV} \end{bmatrix} \begin{bmatrix} 1 & j \\ j & 1 \end{bmatrix} \tag{12}$$

where L and R represent the left circular and right circular respectively. The Faraday rotation angle for a circularly polarized scattering matrix is shown in equation (13) (Shimada, 2019).

$$\Omega = \frac{1}{4} arg\left(M_{LR} M^{*}_{RL}\right) \tag{13}$$

After estimating the Faraday rotation angle Ω using equation (13) it is substituted in equation (11) to derive the scattering matrix $[S]$ free from Faraday rotation error.

Table 3
Channel imbalance and Phase bias values before and after Pol Cal.

Dataset	Co-channel Imbalance (f)			Cross-channel Imbalance (g)			Phase bias (degrees)		
	Ideal	Before PolCal	After PolCal	Ideal	Before PolCal	After PolCal	Ideal	Before PolCal	After PolCal
LS-ASAR L-band dataset	1.0	1.292	0.997	1.0	0.968	1.0	0.0	2.26	−0.726
LS-ASAR S-band dataset	1.0	1.179	0.999	1.0	1.126	1.0	0.0	−0.415	0.222
UAVSAR dataset L-band	1.0	1.394	0.978	1.0	1.128	1.0	0.0	−1.14	−0.629
RADARSAT-2 18-February-2019	1.0	1.25	1.01	1.0	0.90	1.0	0.0	−1.24	0.679
RADARSAT-2 14-March-2019	1.0	1.39	0.98	1.0	1.18	1.0	0.0	2.34	−0.51
ALOS-2 PALSAR-2	1.0	1.05	1.03	1.0	1.0	1.0	0.0	0.3	0.1

3.3. Polarimetric calibration of compact-pol datasets

The polarimetric calibration of compact-pol datasets is more difficult compared to the polarimetric calibration of Quad-pol dataset because of the more number of unknowns in the linear set of equations for solving the polarimetric distortion parameters (Chen and Quegan, 2011; Tan and Hong, 2016). The compact-pol polarimetric calibration algorithm proposed by Freeman (Freeman et al., 2008; Truong-Loï et al., 2010) is adopted for this study. The polarimetric distortion matrix shown in equation (14) includes channel imbalances, crosstalk, and Faraday rotation error (Truong-Loï et al., 2010).

$$\begin{bmatrix} M_{RH} \\ M_{RV} \end{bmatrix} == \frac{1}{\sqrt{2}} \begin{bmatrix} 1 & \delta_2 \\ \delta_1 & f_1 \end{bmatrix} \begin{bmatrix} cos\Omega & sin\Omega \\ -sin\Omega & cos\Omega \end{bmatrix} \begin{bmatrix} S_{HH} & S_{HV} \\ S_{VH} & S_{VV} \end{bmatrix} \begin{bmatrix} cos\Omega & sin\Omega \\ -sin\Omega & cos\Omega \end{bmatrix} \begin{bmatrix} 1 & \delta_1 \\ \delta_2 & f_1 \end{bmatrix} \begin{bmatrix} 1 \\ -j \end{bmatrix} \quad (14)$$

where, δ_1 and δ_2 are the crosstalk parameters, f_1 represents channel imbalance, Ω is the Faraday rotation angle. Due to the circular polarimetric transmission of the signal, no effect of Faraday rotation will occur but the possibility cannot be ignored in the received linearly polarized combinations. The polarimetric of CTLR mode SAR system could be estimated using equations (15)–(18) (Truong-Loï et al., 2010).

$$\delta_1 = \frac{j}{2}\left(\frac{M_{RV}^{*D0}}{M_{RH}^{D0}}\frac{M_{RV}^{D45}}{M_{RH}^{D45}} - \frac{M_{RH}^{D45}}{M_{RV}^{D45}}\frac{M_{RV}^{D0}}{M_{RH}^{D0}}\right) \quad (15)$$

$$f_1 = \frac{2j}{\frac{M_{RH}^{T}}{M_{RV}^{T}} - \frac{M_{RH}^{D45}}{M_{RV}^{D45}}} \quad (16)$$

$$\delta_2 = |f_1|^2 \frac{M_{RH}^{D45*}}{M_{RV}^{D45*}} - \delta_1^* f_1 - j f_1 \quad (17)$$

$$\Omega = \frac{-j}{2} \ln\left(\frac{M_{RH}^{D45}}{M_{RH}^{T}}\left(j\frac{M_{RV}^{D0}}{M_{RH}^{D0}}\frac{M_{RV}^{D45}}{M_{RH}^{D45}} - 2j\right)^{-1}\right) \quad (18)$$

In the above equations $[M]^0$ and $[M]^{D45}$ show a scattering matrices obtained from a Dihedral corner reflector oriented at 0^o and 45^o respectively. After estimating all the polarimetric distortion parameters, the matrix inversion process of the polarimetric distortion matrix (equation (4.34) is done to estimate the scattering matrix free from all polarimetric distortions.

4. Results

The results obtained by performing the polarimetric calibration procedures described in the previous section are described here.

4.1. Polarimetric calibration analysis of the quad-pol datasets

4.1.1. Channel imbalance, phase bias, and crosstalk analysis

Initially, the channel imbalance, phase bias, and crosstalk present in the airborne and spaceborne dataset were estimated and minimized using the methodology explained in the previous section and the results are shown in Tables 3 and 4.

Table 3 shows the channel imbalance and phase bias values estimated before and after channel imbalance and phase bias calibration. The channel imbalances are represented on a linear scale without any unit and the phase bias is represented in degrees. The ideal values for both the co-channel and cross-channel imbalances are 1.0 and the ideal value for phase bias is 0 degrees. By analyzing the Table 3, it can be found that for all the datasets, before channel imbalance calibration itself, both the channel imbalances are close to their ideal values. For the ISRO's LS-ASAR L-band dataset, the co-channel imbalance is more with a deviation of 0.292 from the ideal value and the cross-channel imbalance is almost zero with a deviation of 0.032 from the ideal value. After channel imbalance calibration, the co-channel imbalance deviation is reduced to 0.003 from the ideal value and the cross-channel imbalance is equal to the ideal value. There is a phase bias error of 2.26 degrees before phase bias calibration and after phase bias calibration; it was reduced to −0.726 degrees. For the ISRO's LS-ASAR S-band dataset, the co-channel imbalance and cross-channel imbalances are almost equal with a deviation of 0.179 and 0.126 respectively. After channel imbalance calibration both, the co-channel and cross-channel imbalances are completely removed with their values equal to the ideal values. The phase bias error was −0.415 before phase bias calibration and after phase bias calibration it is now reduced to 0.222.

Table 4
The crosstalk values estimated before and after crosstalk calibration.

Dataset	Uncalibrated Crosstalk (dB)	Residual crosstalk after Quegan method (dB)	Residual crosstalk after Improved Quegan method (dB)	Residual crosstalk after Ainsworth method (dB)
LS-ASAR L-band dataset	−20.28	−26.95	−31.24	−29.11
LS-ASAR S-band dataset	−30.32	−35.96	−42.97	−44.25
L-band UAVSAR dataset	−22.49	−25.33	−30.85	−29.99
RADARSAT-2 18-February-2019	−30.28	−35.61	−48.32	−48.35
RADARSAT-2 14-March-2019	−28.12	−32.48	−46.29	−46.15
ALOS-2 PALSAR-2	−46.25	−46.25	−46.35	−46.27

By analyzing the UAVSAR L-band dataset, the co-channel imbalance is more with a deviation of 0.394 from the ideal value and the cross-channel imbalance is having a deviation of 0.128 from the ideal value. After channel imbalance calibration, the co-channel imbalance deviation is reduced to 0.022 from the ideal value and the cross-channel imbalance is equal to the ideal value. There is a phase bias error of −1.14 degrees before phase bias calibration and after phase bias calibration; it was reduced to −0.629 degrees.

For both the RADARSAT-2 datasets acquired on 18th February 2019 and 14th March 2019, the co-channel imbalance is more with a deviation of 0.25 and 0.39 respectively from their ideal values. After channel imbalance calibration, for the 18th February 2019 dataset the co-channel imbalance deviation from the ideal value reduced to 0.01, and for the 14th March 2019 dataset the channel imbalance deviation reduced to 0.02 from the ideal value. The cross-channel imbalance deviation was 0.1 from the ideal value for the 18th February 2019 dataset before channel imbalance calibration and for the 14th March 2019 dataset, it was 0.18. After channel imbalance calibration, the cross-channel imbalance was completely removed for both the datasets with the cross-channel imbalance value exactly equal to its ideal value. There was a phase bias error of −1.24 degrees for the 18th February 2019 dataset before phase bias calibration and after phase bias calibration, it reduced to 0.679 degrees. Similarly, for the 14th March 2019 dataset, there was a phase bias error of 2.34 degrees before phase bias calibration, and after phase bias calibration the phase bias error was reduced to −0.51 degrees. By comparing the channel imbalances and phase bias before calibration it can be observed that the dataset acquired on 14th March 2019 is slightly more polarimetrically distorted than the dataset acquired on 18th February 2019. From Table 3, it can be seen that for the ALOS-2 PALSAR-2 the co-channel imbalance, cross-channel imbalance, and phase bias are negligible and almost equal to the ideal values. This is because the dataset is already polarimetrically calibrated by JAXA before data dissemination (ESA, 2014).

Table 4 shows the crosstalk values estimated before and after crosstalk calibration. The crosstalk values are expressed in decibel units and as per the system design requirement of most of the SAR sensors, the crosstalk should be less than −30 dB. From the Table 4, it can be observed that before crosstalk calibration the L-band LS-ASAR dataset is affected with a very high crosstalk of −20.28 dB. After crosstalk calibration using the Quegan algorithm, the crosstalk reduced to −26.95 dB. Therefore, the Quegan algorithm was able to reduce the crosstalk by a magnitude of 6.67 dB. The Improved Quegan algorithm was able to reduce the crosstalk to −31.24 dB making a difference of 10.96 dB to the crosstalk level. The Ainsworth algorithm reduced the crosstalk by 8.83 dB to a lower level of −29.11 Db. Therefore, for the LS-ASAR L-band dataset, the Improved Quegan algorithm was able to reduce

the crosstalk to the lowest level of −31.24 dB out of all the three algorithms.

For the LS-ASAR S-band dataset, it can be seen that before polarimetric calibration itself, the crosstalk present in the dataset is −30.32 dB, which is in the allowable limit. By comparing the crosstalk present in the uncalibrated L-band LS-ASAR dataset shown in Table 4, it can be found that the S-band LS-ASAR dataset is well calibrated in contrast to the L-band LS-ASAR dataset. After crosstalk calibration using the Quegan algorithm, the crosstalk reduced to −35.96 dB. Therefore, the Quegan algorithm was able to reduce the crosstalk by a magnitude of 5.64 dB. The Improved Quegan algorithm was able to reduce the crosstalk to −42.97 dB making a difference of 12.65 dB to the crosstalk level. The Ainsworth algorithm reduced the crosstalk by 13.93 dB to a lower level of −44.25 dB. So for the LS-ASAR S-band dataset, the Ainsworth algorithm showed a reduced crosstalk to a lowest level of −44.25 dB out of all the three algorithms.

From Table 4, it can be observed that before crosstalk calibration the L-band UAVSAR dataset is affected with very high crosstalk of –22.49 dB. After crosstalk calibration using the Quegan algorithm, the crosstalk reduced to −25.33 dB. Therefore, the Quegan algorithm was able to reduce the crosstalk by a magnitude of 2.84 dB. The Improved Quegan algorithm was able to reduce the crosstalk to –30.85 dB making a difference of 8.36 dB to the crosstalk level. The Ainsworth algorithm reduced the crosstalk by 7.5 dB to a lower level of −29.99 dB. So for the UAVSAR L-band dataset, the Improved Quegan algorithm was able to reduce the crosstalk to the lowest level of −30.85 dB out of all the three algorithms. It can be seen from Table 4 that before polarimetric calibration itself, the crosstalk present in the dataset acquired on 18th February 2019 is −30.32 dB which is in the allowable limit. The dataset acquired on 14th March 2019 is having more crosstalk of −28.12 dB. For the 18th February 2019 dataset, after crosstalk calibration using the Quegan algorithm, the crosstalk was reduced to −35.61 dB. So the Quegan algorithm was able to reduce the crosstalk by a magnitude of 5.33 dB. The Improved Quegan algorithm was able to reduce the crosstalk to −48.32 dB making a difference of 18.04 dB to the crosstalk level. The Ainsworth algorithm reduced the crosstalk by 18.07 dB to a lower level of −48.35 dB. For the 14th March 2019 dataset, after crosstalk calibration using the Quegan algorithm, the crosstalk was reduced to –32.48 dB. So the Quegan algorithm was able to reduce the crosstalk by a magnitude of 4.36 dB. The Improved Quegan algorithm was able to reduce the crosstalk to −46.29 dB making a difference of 18.17 dB to the crosstalk level. The Ainsworth algorithm reduced the crosstalk by 18.03 dB to a lower level of −46.15 dB. So for the 18th February 2019 dataset, the Ainsworth algorithm was able to show a slightly better performance over the Improved Quegan algorithm, and for the 14th March 2019 dataset, the Improved Quegan algorithm was able to provide slightly better performance over the Ainsworth algorithm. From Table 4, it can be observed that for the ALOS-2 PALSAR-2 before polarimetric calibration the crosstalk is of very low magnitude (-46.25 dB) and there occurred no considerable change to the crosstalk level after crosstalk calibration using Quegan, Improved Quegan and Ainsworth algorithm. This points out to the efficient polarimetric calibration done by JAXA before data distribution.

4.1.2. Trihedral corner reflector polarimetric signature-based analysis

Polarimetric signature is a graphical way to represent the received power as a function of polarization. The polarimetric signature is represented in a four-dimensional space because the polarization of the horizontal and vertical antennas can be varied independently. So polarimetric signature is plotted by representing two polarizations as a function of the orientation angle and ellipticity angle of the polarization ellipse (Van Zyl and Kim, 2011). So, for quad-pol data, two polarimetric signatures can be plotted- the co-polarized polarimetric signature and the cross-polarized polarimetric signature. The co-polarized polarimetric signature represents the HH & VV channels while the cross-polarized polarimetric signature represents the HV & VH polarizations. In the three dimensional representation of the polarimetric signature, the z-axis indicates the Normalized Radar Cross Section (RCS) on a 0 to 1 scale., the X-axis represents the ellipticity angle ranging from −45 to +45 degrees and the y-axis represents the orientation angle ranging from 0 to 180 degrees (Van Zyl and Kim, 2011).

Polarimetric signatures can be used as a means for evaluating the quality of the polarimetric calibration by comparing the theoretical polarimetric signatures of the corner reflectors with the polarimetric signatures of the same corner reflector generated from the datasets before and after calibration (Chang et al., 2018; Fore et al., 2015; Moriyama, 2015). The theoretical polarimetric signatures of a Trihedral corner reflector is shown in Fig. 9.

By observing the polarimetric signatures extracted from the LS-ASAR L-band dataset shown in Fig. 10, the polarimetric signatures before polarimetric calibration are highly distorted. The co-polar polarimetric signature is more distorted compared to the cross-polar polarimetric signatures, which indicate that the HH & VV polarizations are more affected by polarimetric distortions compared to the HV & VH channels. It can be seen that there occurred considerable improvement in both the co-polar and cross-polar polarimetric signatures after crosstalk calibration using the Quegan algorithm. Even though there is an improvement in the polarimetric signatures, the polarimetric signatures are still distorted when compared to the theoretical signatures. By comparing the polarimetric signature with the theoretical signature in Fig. 9, it can be seen that after crosstalk calibration using the Improved Quegan algorithm, both the co-polar and cross-polar signatures are perfectly matching with the theoretical polarimetric signature.

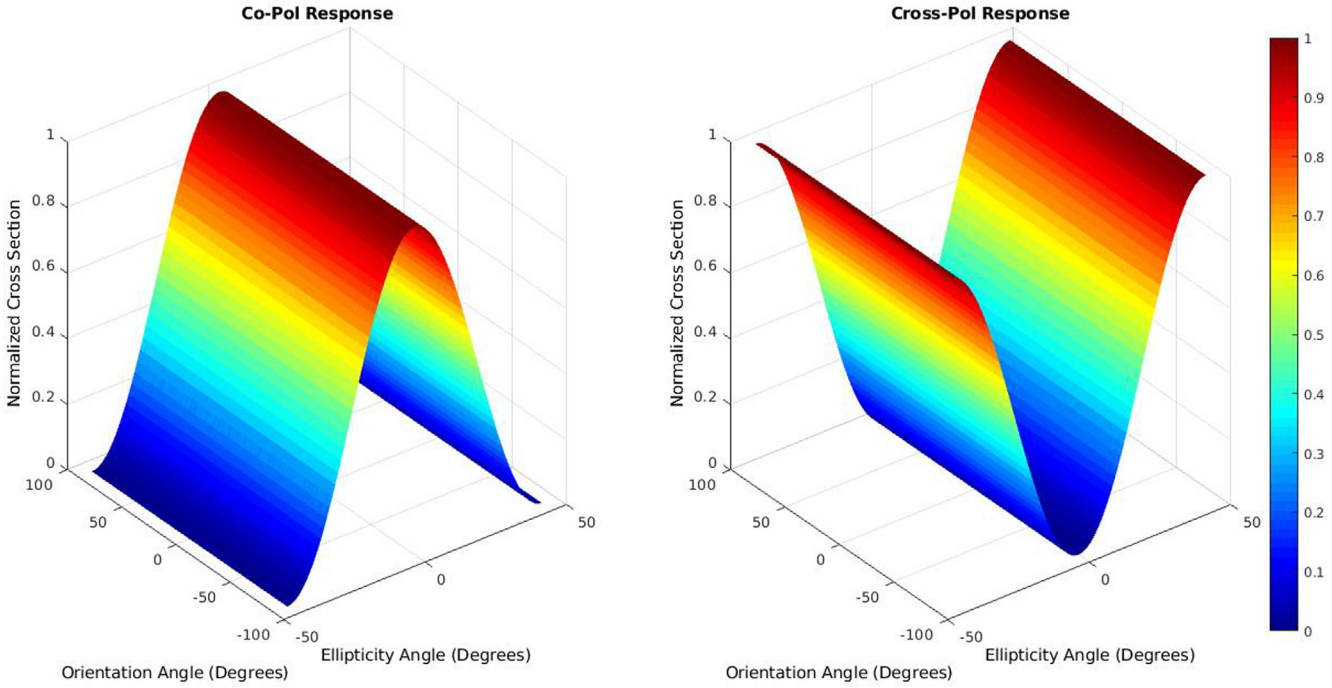

Fig. 9. Theoretical polarimetric signature expected from a Trihedral corner reflector.

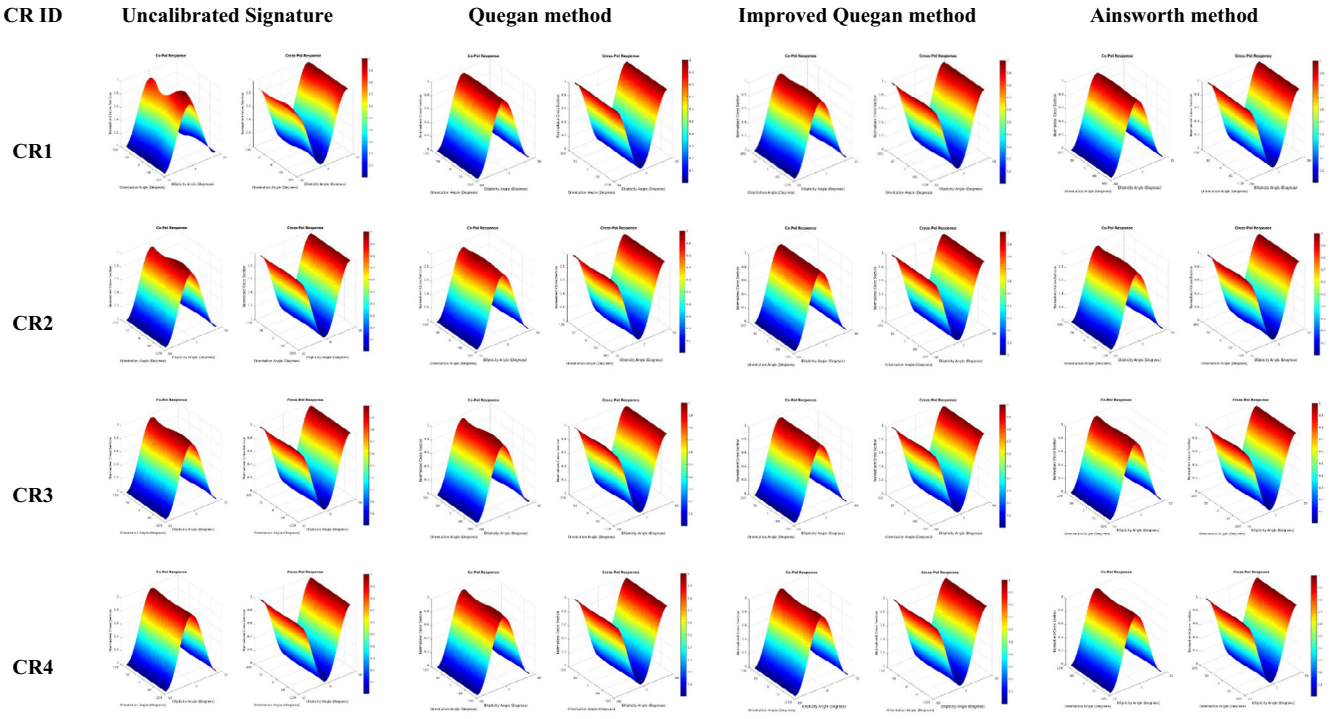

Fig. 10. Polarimetric Signatures of Trihedral corner reflectors extracted from 18-February-2019 RADARSAT-2 dataset.

So it can be said that the crosstalk error is the more dominant polarimetric distortion in the L-band LS-ASAR dataset and the Improved Quegan algorithm was successful in minimizing the crosstalk distortions. By comparing both the co-polar and cross-polar polarimetric signatures with Fig. 10 and Fig. 9, it can be observed that there is a significant improvement in the polarimetric signatures after Ainsworth calibration. However, when comparing with the polarimetric signature generated after crosstalk calibration using the Improved Quegan algorithm shown in Fig. 10, the polarimetric distortions are more in the dataset generated after Ainsworth calibration.

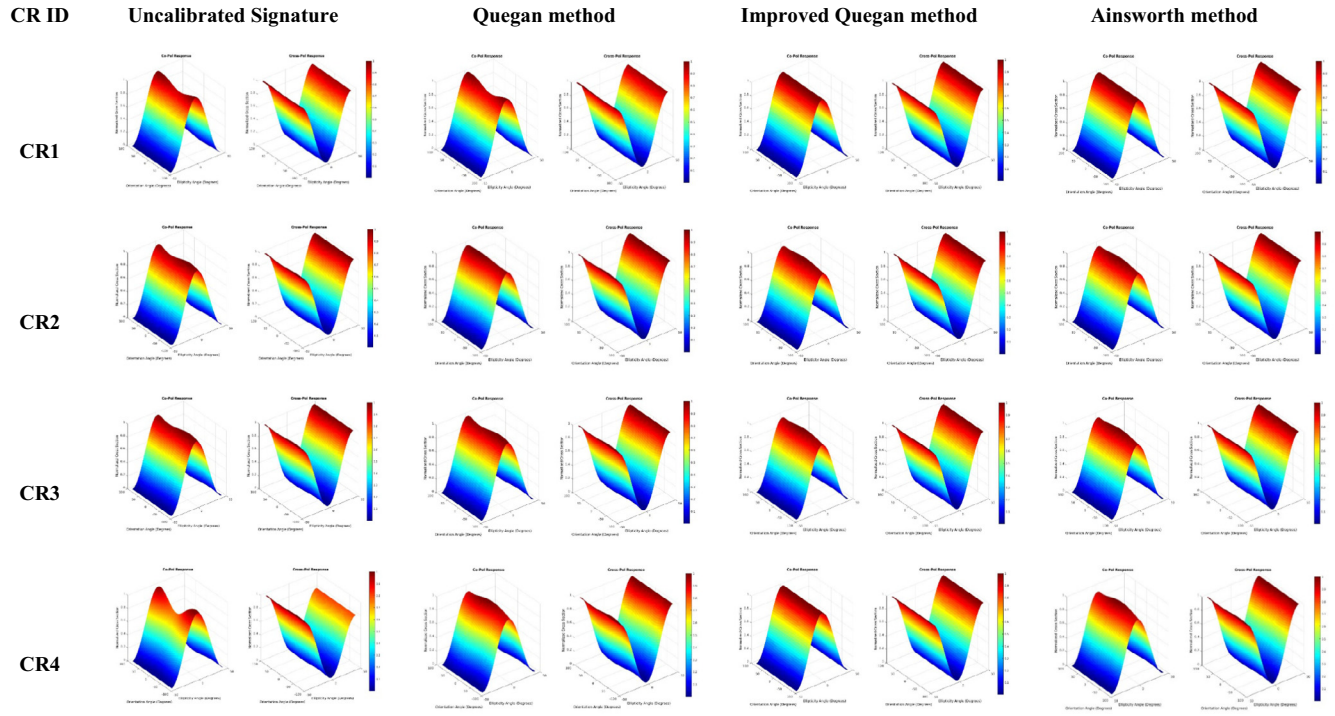

Fig. 11. Polarimetric Signatures of Trihedral corner reflectors extracted from 14-March-2019 RADARSAT-2 dataset.

By analyzing the polarimetric signatures shown in Fig. 10 after polarimetric calibration using Quegan algorithm the co-polar and cross-polar polarimetric signature of the CR1 corner reflector which was highly distorted before polarimetric calibration are now exactly identical to the theoretical polarimetric signature shown in Fig. 9. There is very less improvement in the polarimetric signatures of the CR2 & CR3 corner reflectors after Quegan crosstalk calibration which was less distorted before polarimetric calibration. The polarimetric signature of the CR4 corner reflector which was not distorted before polarimetric calibration got slightly distorted after polarimetric calibration using Quegan algorithm which indicates the wrong estimation of crosstalk by the Quegan algorithm. The polarimetric signature analysis of the trihedral corner reflectors shown in Fig. 9 after polarimetric calibration using Improved Quegan algorithm reveals that all the polarimetric signatures are now closely matching with its theoretical polarimetric signature shown in Fig. 9. This points out that the Improved Quegan algorithm performed well in minimizing the crosstalk from the dataset. The CR2 & CR3 polarimetric signatures are now exactly identical to the theoretical polarimetric signature. The CR1 & CR4 polarimetric signatures are also almost identical to the theoretical polarimetric signature. So the Improved Quegan algorithm was able to minimize both higher and lower levels of crosstalk. By analyzing the polarimetric signatures of the trihedral corner reflectors after polarimetric calibration using Ainsworth algorithm (shown in Fig. 10), it can be understood that the polarimetric signatures are closely matching with the theoretical polarimetric signatures shown in Fig. 9. So similar to the Improved Quegan algorithm, the Ainsworth method is also capable to minimize the crosstalk effectively from the dataset.

Fig. 11 shows the polarimetric signatures of the triangular trihedral corner reflector extracted from the RADARSAT-2 dataset acquired on 14th March 2019 before polarimetric calibration and after polarimetric calibration using Quegan algorithm, Improved Quegan algorithm and Ainsworth algorithm. By analyzing the polarimetric signatures from the four trihedral corner reflectors before polarimetric calibration, it can be seen that the co-polar polarimetric signature of the CR1 & CR4 corner reflectors are highly distorted. For the CR2 & CR3 corner reflectors, the co-polar polarimetric signatures before polarimetric calibration are having a small amount of distortions when compared to the identical co-polar polarimetric signature shown in Fig. 9. By analyzing the figure, it can be understood that the CR4 polarimetric signature, which was highly distorted before polarimetric calibration, got significantly Improved and now almost similar to the theoretical polarimetric signature. The CR2 & CR3 polarimetric signatures are now significantly Improved and now looks almost similar to the theoretical polarimetric signature. There is no considerable improvement visible for the polarimetric signature of the CR1 corner reflector after polarimetric calibration using Quegan algorithm. Fig. 10 also contains the polarimetric signatures of the trihedral corner reflectors extracted from the dataset after polarimetric calibration using Improved Quegan algorithm. By analyzing and comparing the polarimetric signatures with the theoretical polarimetric signatures, it can be understood that the crosstalk was the reason for the distortions in the polarimetric signatures and after polarimetric calibration using Improved Quegan algorithm, the polarimetric signatures were behaving

close to the theoretical signatures. Similarly, Fig. 10 also shows the polarimetric signatures after polarimetric calibration using Ainsworth algorithm, these signatures were also closely matching with the theoretical polarimetric signatures. By comparing the polarimetric signatures after polarimetric calibration using Improved Quegan algorithm and Ainsworth algorithm, it can be found that the signatures generated after Improved Quegan algorithm are slightly better than the Ainsworth algorithm because of more match with the identical polarimetric signature. For the ALOS-2 PALSAR-2 dataset, the polarimetric signature generated before polarimetric calibration (Fig. 12) is exactly matching with the ideal polarimetric signature of the trihedral corner reflector shown in Fig. 9. There occurred no change to the polarimetric signature after crosstalk calibration using the three available algorithms.

By analyzing both the co-polar and cross-polar polarimetric signatures for the LS-ASAR S-band dataset shown in Fig. 12, it can be said the co-polar polarimetric signature is highly distorted and the cross-polar polarimetric signature is having only very small distortion which indicates that HH & VV channels are having more distortions compared to the HV & VH channels. The uncalibrated polarimetric signatures of the S-band LS-ASAR dataset are having less distortion compared to the uncalibrated polarimetric signatures of the L-band LS-ASAR dataset. It can be seen that there occurred considerable improvement in the co-polar polarimetric signature after crosstalk calibration using the Quegan algorithm. The cross-polar polarimetric signature remains unchanged. Even though there is an improvement in the co-polar polarimetric signature, the polarimetric signature is still distorted when compared to the theoretical signature. By comparing the polarimetric signature with the theoretical signature, it can be seen that after crosstalk calibration using the Improved Quegan method and Ainsworth method, both the co-polar and cross-polar signatures are perfectly matching with the theoretical polarimetric signature

For the L-band UAVSAR dataset, the co-polar polarimetric signature before polarimetric calibration is more distorted compared to the cross-polar polarimetric signatures which indicate that the HH & VV polarizations are more affected by polarimetric distortions compared to the HV & VH channels. The same trend is observed for the L&S Band Airborne SAR datasets also. From Fig. 10, it can be seen that there occurred considerable improvement in both the co-polar and cross-polar polarimetric signatures after crosstalk calibration using the Quegan algorithm. The cross-polar polarimetric signature is now exactly matching with the theoretical cross-polar polari-

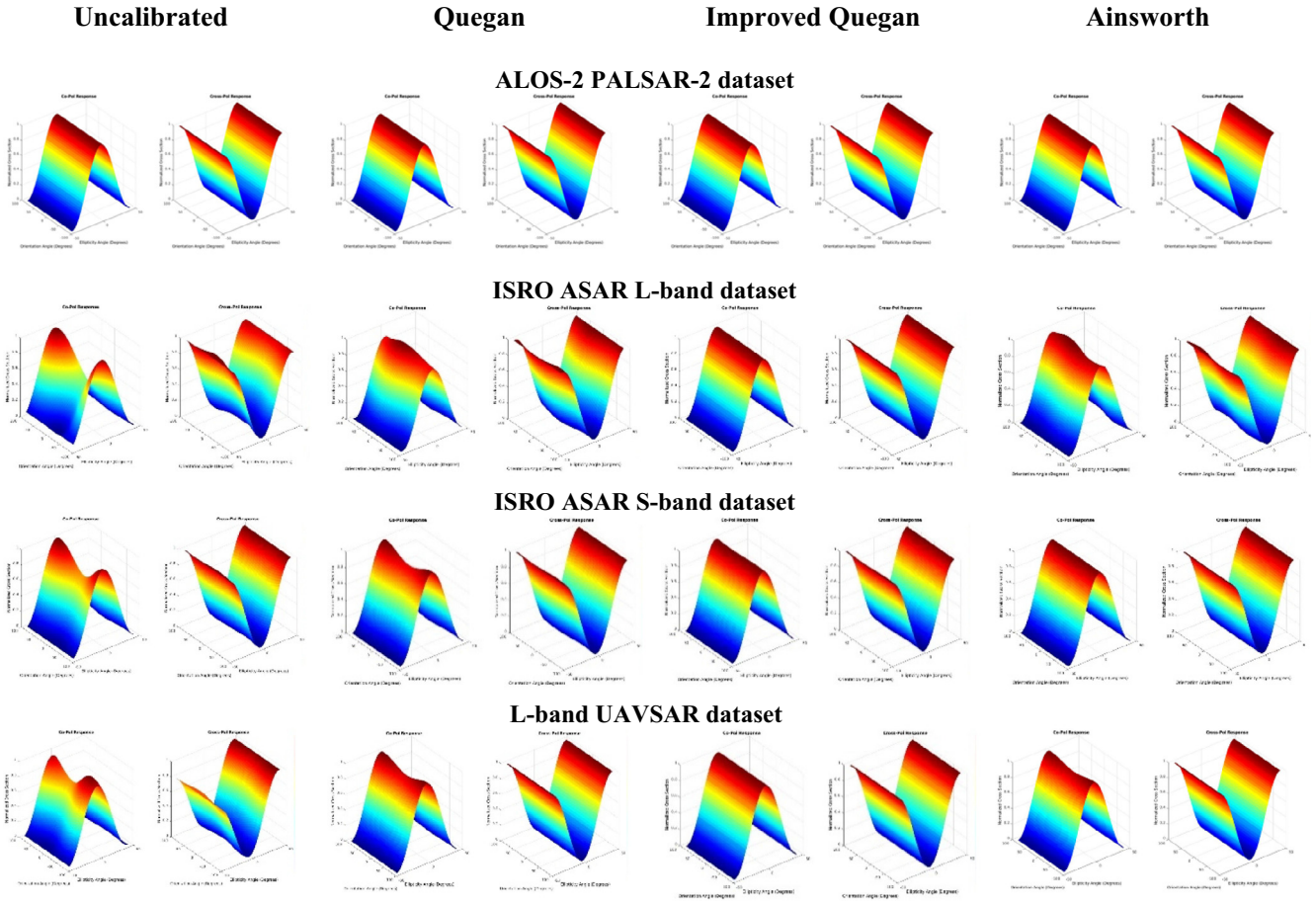

Fig. 12. Polarimetric signatures extracted from the Quad-pol datasets.

metric signature expected from a triangular trihedral corner reflector. Even though there is an improvement in the co-polar polarimetric signature, the polarimetric signature is still distorted when compared to the theoretical signatures. After crosstalk calibration using the Improved Quegan algorithm, both the co-polar and cross-polar signatures are perfectly matching with the theoretical polarimetric signature. By comparing both the co-polar and cross-polar polarimetric signatures, it can be observed that there is a significant improvement in the polarimetric signatures after Ainsworth calibration. However, the polarimetric distortions are more when compared with the Improved Quegan algorithm.

For the ALOS-2 PALSAR-2 dataset, the polarimetric signature generated before polarimetric calibration is exactly matching with the ideal polarimetric signature of the trihedral corner reflector shown in Fig. 9. There occurred no change to the polarimetric signature after crosstalk calibration using the three available algorithms.

4.1.3. Coherency and scattering matrix based analysis

Fig. 13a–c shows the diagonal elements of the 3x3 coherency matrix before polarimetric calibration showing a triangular trihedral corner reflector. In the 3x3 Coherency matrix, the first diagonal element T11 represents odd bounce (surface) scattering, the second diagonal element T22 represents the double bounce scattering and the third diagonal element T33 represents the volume scattering (Kumar et al., 2016a). Since the triangular trihedral corner reflector is having three side plates, the incident EM wave on the corner reflector surface is subjected to three times reflection. Therefore, a trihedral corner reflector should be visible only in the T11 image of the 3x3 Coherency matrix. However, in Fig. 13, the triangular trihedral corner reflector is visible in both T11 & T22 images, which indicates that the corner reflector is exhibiting both odd bounce and double bounce scattering behavior. Due to the orientation of triangular trihedral corner reflector the decomposition of the particular resolution cell should highlight odd-bounce scattering. The odd-bounce scattering element is mainly highlighted by the first diagonal element of the coherency matrix (Kumar, 2019). Fig. 13d–f shows the diagonal elements of the 3x3 coherency matrix of the L-band LS-ASAR dataset showing the image of a triangular trihedral corner reflector after polarimetric calibration using Improved Quegan algorithm which performed best for reducing the crosstalk.

From a comparison of Fig. 13e with Fig. 13b, it can be observed that the corner reflector brightness in the T22 diagonal image representing the double bounce scattering is considerably reduced in Fig. 13e which indicates the improvement in ground target characterization after polarimetric calibration. Fig. 14 shows the correlation scatter plots between the scattering matrix elements of the dataset. As per the theory, a monostatic radar that uses the same antenna for signal transmission and reception should obey the scattering reciprocity condition, i.e. the HV channel should be equal to the VH channel. However, by analyzing Fig. 14a it can be seen that the HV channel is not equal to the VH channel violating the scattering

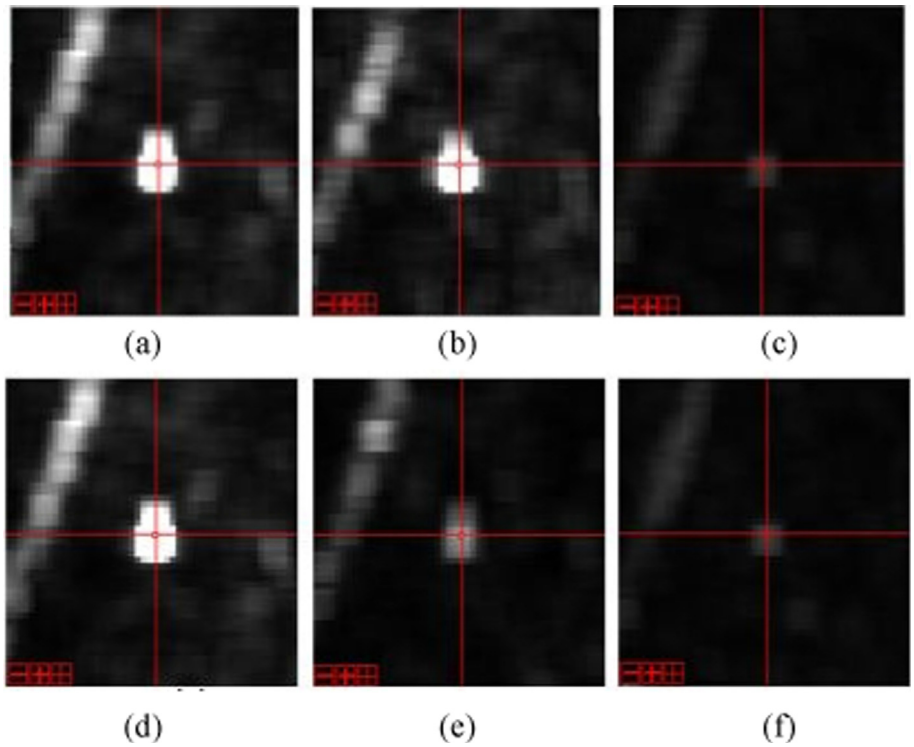

Fig. 13. Coherency Matrix elements; (a) T11 before PolCal; (b) T22 before PolCal; (c) T33 before PolCal; (d) T11 after PolCal; (e) T22 after PolCal; (f) T33 after PolCal.

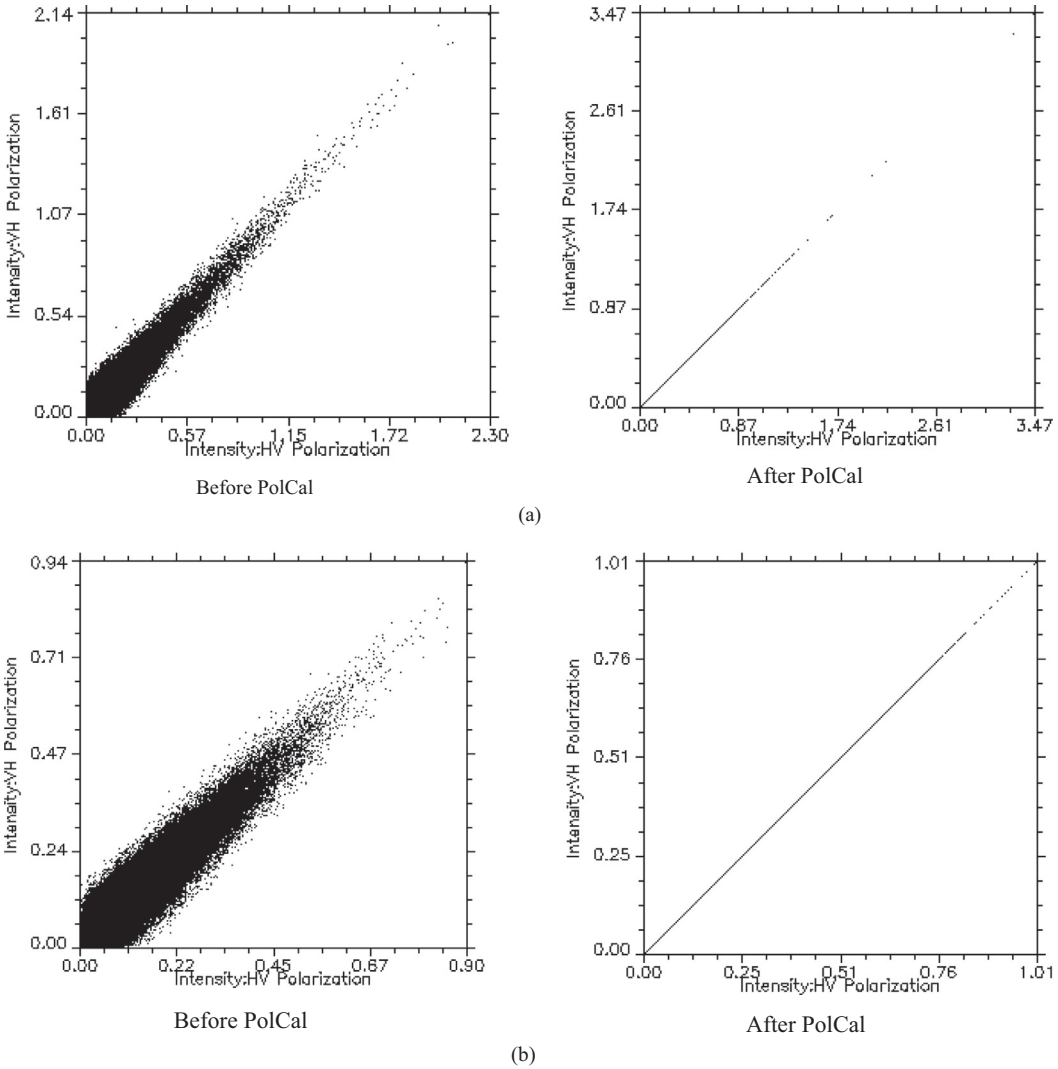

Fig. 14. Correlation scatter plot between HV & VH of spaceborne SAR sensors; (a) C- band RADARSAT-2 dataset acquired on 18th February 2019 (b) L-band ALOS-2 PALSAR-2.

reciprocity. Fig. 14b shows the correlation scatter plots of the dataset after polarimetric calibration using the Improved Quegan algorithm. By comparing Fig. 14a with Fig. 14b it can be seen that after polarimetric calibration, the HV & VH channels of the dataset are perfectly obeying the scattering reciprocity condition indicated by the straight-line correlation plot between the channels.

Fig. 14a, b shows the correlation scatter plots between the scattering matrix elements of the RADARSAT-2 and ALOS-2 PALSAR-2 datasets. By comparing Fig. 14a, b, it can be seen that after polarimetric calibration, the HV & VH channels of the dataset are perfectly obeying the scattering reciprocity condition indicated by the straight line correlation plot between the channels. Therefore, the violation of the scattering reciprocity condition before polarimetric calibration was solely due to the polarimetric distortions present in the dataset.

Fig. 15 shows the correlation scatter plots of the dataset after polarimetric calibration of the ISRO's L&S Band Airborne SAR and L-band UAVSAR dataset using the Improved Quegan algorithm. It can be seen that after polarimetric calibration, the HV & VH channels of the dataset are perfectly obeying the scattering reciprocity condition indicated by the straight line correlation plot between the channels.

4.1.4. Roll invariant parameter-based analysis

The dominant scattering-type magnitude parameter (α_s1) is a roll invariant parameter, which is independent of the orientation angle of the EM wave and it is generated as a part of Touzi decomposition (Touzi, 2017, 2007). The α_s1 parameter indicates the dominant scattering mechanism from the ground target present at a location. The α_s1 value of 0 indicates odd bounce (surface) scattering, 45 indicates volume scattering and 90 indicates double-bounce scattering (Gosselin et al., 2014; Touzi et al., 2009). Table 5 shows the α_s1 values estimated for different ground targets before and after polarimetric calibration

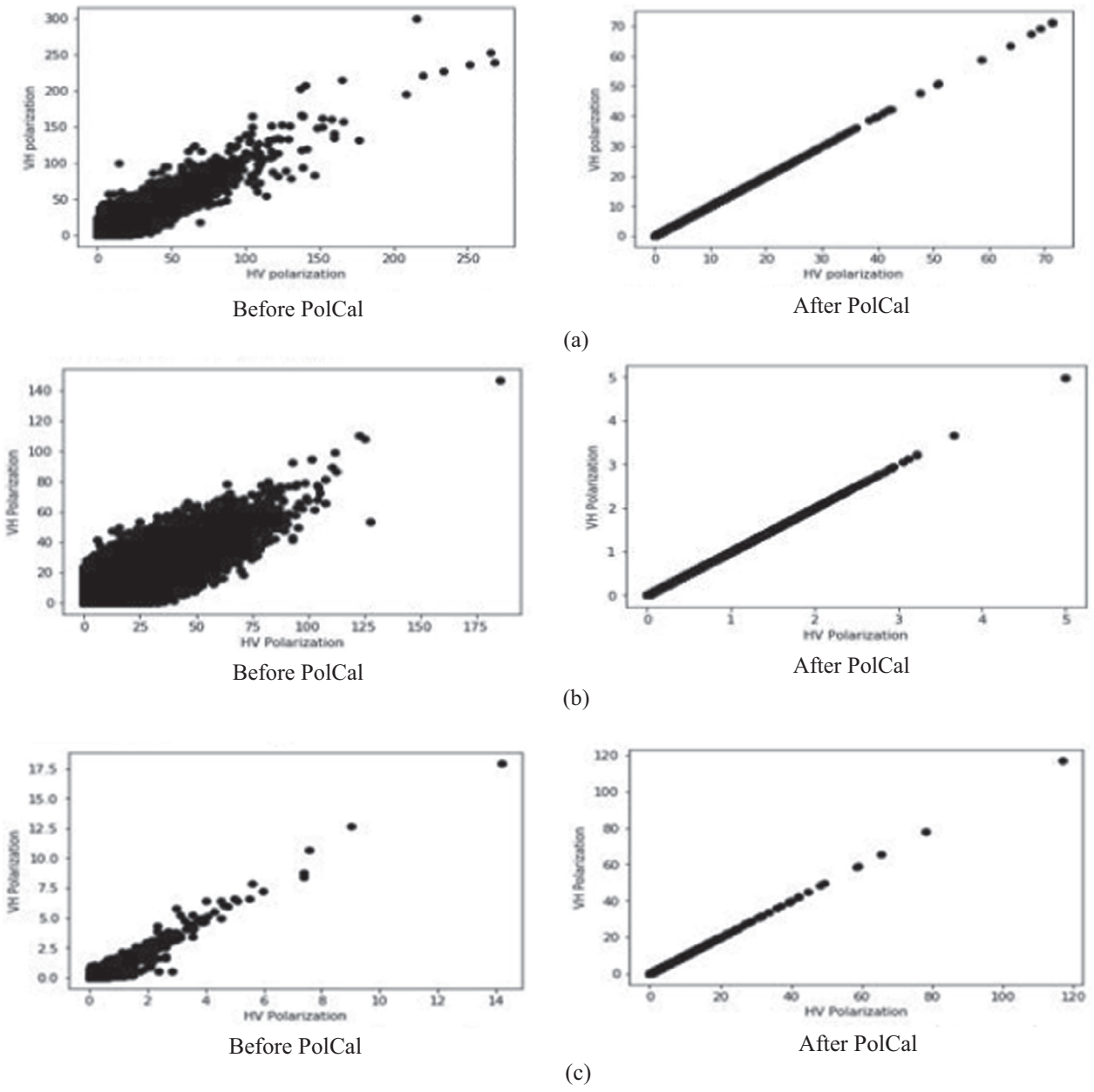

Fig. 15. Correlation scatter plot between HV & VH of airborne SAR sensors; (a) ISRO's L-band Airborne SAR dataset (b) ISRO's S-band Airborne SAR dataset (c) L-band UAVSAR dataset.

Table 5
α_s1 value for different ground targets estimated from ISRO's L-band LS-ASAR dataset.

Scatterer	Theoretical α_s1 value	α_s1 value before Pol Cal	α_s1 value after Pol Cal
Dihedral CR	90	71.78	74.77
Trihedral CR	0	19.05	5.80
Barren land	0	41.02	11.62
Vegetation	45	24.59	47.10

and their theoretical values. By analyzing the results for LS-ASAR data, it can be found that before polarimetric calibration, the barren lands were giving a high amount of volume scattering with α_s1 of 41.02 and appearing in yellow color in the image, and the vegetated areas were showing surface scattering behavior with α_s1 of 24.59 and appearing in blue color in the image. The Dihedral and Trihedral corner reflectors were also showing a α_s1 of 71.78 and 19.05 respectively, which were having large deviations from their theoretical values. By analyzing

Table 6
α_s1 value for different ground targets estimated from ISRO's S-band LS-ASAR dataset.

Scatterer	Theoretical α_s1 value	α_s1 value before Pol Cal	α_s1 value after Pol Cal
Dihedral CR	90	55.90	66.70
Trihedral CR	0	6.67	2.17
Barren land	0	20.03	11.11
Vegetation	45	16.63	10.33

Table 5, it can be seen the α_s1 of barren lands is now considerably Improved to 11.62 representing surface scattering behavior and is appearing in blue color. The vegetation is also showing a α_s1 of 47.10 representing volume scattering behavior and is appearing in yellow color. The α_s1 of Dihedral and Trihedral corner reflectors are now improved to 74.77 and 5.80 respectively behaving more closely to their expected theoretical α_s1 values.

Table 6 shows the α_s1 values estimated for different ground targets before and after polarimetric calibration and their theoretical values. By analyzing Table 6, it can be found that before polarimetric calibration, the barren lands were exhibiting the wrong scattering mechanism with α_s1 of 20.03 appearing in yellow color, and the vegetated areas were showing surface scattering behavior with α_s1 of 16.63 and appearing in blue color in the image. The Dihedral and Trihedral corner reflectors were also showing a α_s1 of 55.90 and 6.67 respectively, which were having large deviations from their theoretical values.

By analyzing Table 6, it can be seen the α_s1 of barren lands is now considerably improved to 11.11 representing surface scattering behavior and is appearing in blue color. The vegetation is showing a α_s1 of 10.33 representing surface scattering behavior, which is wrong as per theory, and the reasons need to be investigated. The α_s1 of Dihedral and Trihedral corner reflectors are now improved to 66.70 and 2.17 respectively behaving more closely to their expected theoretical α_s1 values.

From Table 7, it can be seen that the α_s1 values for the Trihedral CR, barren land, and vegetation extracted from the L-band UAVSAR and RADASAT-2 datasets deviated from their theoretically expected α_s1 values and after polarimetric calibration, the α_s1 values were closely matching with their theoretical values. For the ALOS-2 PALSAR-2 dataset, since it is already polarimetrically calibrated, the α_s1 values of the three different targets are closely matching with the theoretical values, and only very little change has been noticed after polarimetric calibration.

4.1.5. Faraday rotation analysis

In contrast to the airborne SAR sensors, the RADARSAT-2 spaceborne SAR sensor is also subjected to the atmosphere induced polarimetric distortion caused mainly due to the Earth's ionosphere known as the Faraday rotation. Similar to crosstalk, the Faraday rotation also leads to the leakage of co-polarized signal power to the cross-polarized channels, so in addition to the system induced polarimetric distortions, the Faraday rotation error also needs to be estimated and minimized. Since the Faraday rotation causes a polarimetric distortion effect identical to crosstalk, Faraday rotation is estimated only after removing the crosstalk from the datasets. However, the C-band EM wave frequency in which the RADARSAT-2 operates is less affected by Faraday rotation, it can be considered negligible. Table 8 shows the Faraday rotation angles estimated for the two RADARSAT-2 and the ALOS-2 PALSAR-2 datasets after performing polarimetric calibration for the system induced polarimetric distortions.

Since the two RADARSAT-2 datasets were acquired before sunrise at 6.17 am, the Total Electron Content (TEC) of the ionosphere was very low and as expected for C-band the Faraday rotation angles estimated from both the datasets are close to zero, which can be neglected. By analyzing the Table 8, it can be understood that the Faraday rotation angle estimated after crosstalk calibration using the Quegan algorithm is significantly higher than the Faraday rotation angle estimated after crosstalk calibration using the Improved Quegan and Ainsworth algorithm. This is due to the presence of more amount of residual crosstalk in the dataset even after crosstalk calibration using the Quegan algorithm, so this also indicates the inefficiency of the Quegan algorithm in minimizing the crosstalk. In addition, the Faraday rotation angle estimated after crosstalk calibration using Improved Quegan and Ainsworth algorithm shows that the dataset acquired on 14th March 2019 is having a slightly higher amount of Faraday rotation angle compared to the 18th February 2019 dataset, but the Faraday rotation angle estimated after Quegan algorithm is showing the reverse result. The residual crosstalk after the Quegan algorithm affects the Faraday rotation angle calculation, which results in an overestimation of the Faraday rotation angle. The Faraday rotation angles estimated after crosstalk calibration using Improved Quegan and Ainsworth algorithms shows almost similar values, which indicates their similar performance for crosstalk removal.

As per the theory, the L-band ALOS-2 PALSAR-2 dataset should be highly affected by the Faraday rotation error (Wright et al., 2003). But, since the dataset is acquired over the Rio Branco region near to the equator and parallel to the geomagnetic line the linearly polarized L-band electromagnetic waves are not affected by the Faraday rotation effect (Moriyama et al., 2007). The dataset was also calibrated by JAXA for Faraday rotation error, so there is

Table 7
α_s1 value for different ground targets.

Dataset	α_s1 value of Trihedral CR			α_s1 value of Barren land			α_s1 value of Vegetation		
	Theoretical	Before Calibration	After PolCal	Theoretical	Before Calibration	After PolCal	Theoretical	Before Calibration	After PolCal
L- band UAVSAR	0	3.66	1.26	0	9.52	7.19	45	47.95	46.32
RADARSAT-2 (18-February-2019)		1.06	0.58		3.65	1.90		42.29	44.80
RADARSAT-2 (14-March-2019)		4.73	1.59		5.88	2.16		47.89	45.91
ALOS-2 PALSAR-2		0.87	0.75		7.54	6.11		45.45	45.40

no Faraday rotation effect present in the dataset (ESA, 2014).

4.2. Polarimetric calibration analysis for compact-pol datasets

The results obtained from the polarimetric calibration (PolCal) of ISRO's L&S Band Airborne SAR and RISAT-1 compact-pol datasets are explained here.

4.2.1. Polarimetric distortion parameter analysis

The Freeman calibration algorithm-based polarimetric distortion parameters of CTLR mode data in Table 9.

Since RISAT-1 was operated in C-band and the signal transmission was done in circular polarization, the Faraday rotation angle is very small of 0.01927 degrees, which is negligible. By analyzing the magnitude of the polarimetric distortions of the ISRO's L&S Band Airborne SAR datasets shown in the Table 9, it can be understood that the crosstalk is more in the L-band dataset compared to the S-band dataset. It is indicated by the higher values of complex crosstalk parameters δ_1 & δ_2 in Table 9. The channel imbalance is higher in the S-band dataset compared to the L-band dataset indicated by the higher value of channel imbalance parameterf_1. Since the datasets were acquired using the airborne platform, there is no possibility of Faraday rotation error leading to the Faraday rotation angle of zero degrees.

4.2.2. Cloude compact –pol model-based polarimetric decomposition analysis

An analysis was done with Cloude decomposition-based results of polarimetrically uncalibrated and calibrated scattering matrices of RISAT-1 data and the color composite images are shown in Fig. 16. The double-bounce scatterers are represented in red color, surface scattering is highlighted in blue color and green shows the dominance of volume scattering in the decomposition-based color composite image (Fig. 16)

From Fig. 16a it can be found that the barren lands present at the study area are appearing in red shade indicating the dominance of double-bounce scattering which is wrong as per theory. The absence of blue color at these barren lands indicates the missing surface scattering mechanism. The sparse vegetation present at the area of interest is also appearing in cyan color which indicates the equal dominance of volume scattering and surface scattering mechanisms. This is also wrong as per theory because for C-band the sparse vegetated should appear in green and yellow color due to volume and double-bounce scattering from land to tree interactions. The thick vegetation present on the East side of the water body is appearing in cyan color indicating equal dominance of surface scattering along with volume scattering. It could be easily seen from Fig. 16 that the smooth surface, which was highlighted as double-bounce scatterers in the decomposition-based result

Table 8
Faraday rotation analysis for the RADARSAT-2 and ALOS-2 PALSAR-2 datasets.

Datasets	FR after Quegan method	FR after Improved Quegan method	FR after Ainsworth method
RADARSAT-2 18-February-2019	−0.0144	−0.00484	−0.0061
RADARSAT-2 14-March-2019	−0.0128	−0.00504	−0.0065
ALOS-2 PALSAR-2	0.0025	0.0023	0.0022

Table 9
Polarimetric distortions parameters estimated from the compact-pol datasets.

Dataset	Complex Crosstalk Parameter 'δ_1'	Complex Crosstalk Parameter 'δ_2'	Channel Imbalance Parameter 'f_1'	Faraday Rotation angle 'Ω'
RISAT-1	0.8715 + 0.2086j	−0.0770–0.1996j	−0.9576 + 0.6808j	0.01927 degrees
ISRO L-band	1.02 + 1.53j	−2.13–0.086j	−0.092 + 0.94j	0 degrees
ISRO S-band	−0.327 + 0.377j	0.512–0.029j	−0.57–0.826j	0 degrees

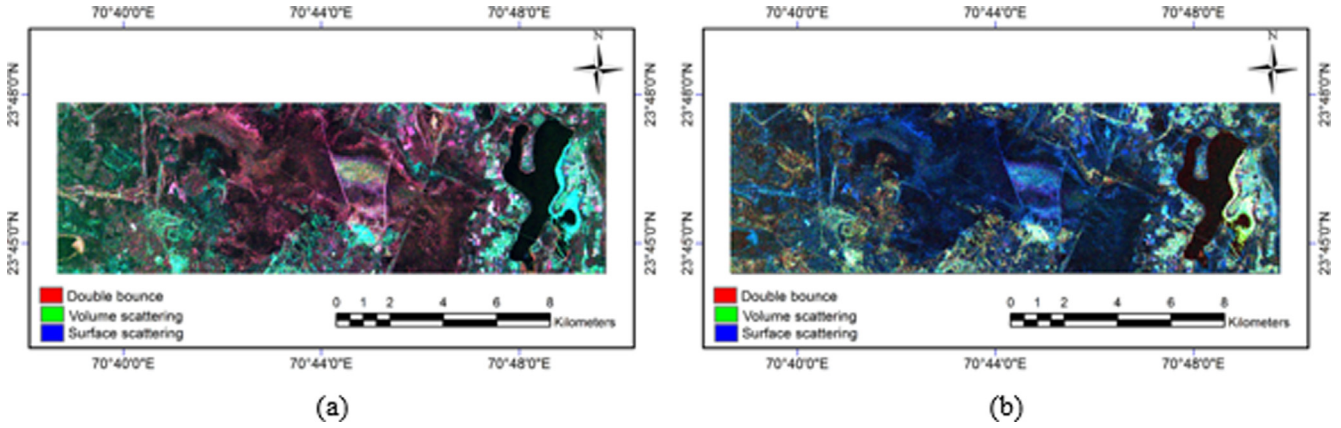

Fig. 16. RGB Composites generated from Cloude compact-pol decomposition of RISAT-1; (a) Before PolCal; (b) After PolCal.

of uncalibrated data, is now appearing as surface scatterer in blue color in the calibrated data.

Fig. 17a shows the scattering magnitudes at the dB scale for a smooth surface of the uncalibrated L-band ISRO's LS-ASAR data and Fig. 17b shows the same graph for the calibrated data. An analysis of both the graphs suggests that the smooth surface, which was misidentified as a double-bounce scatterer in the uncalibrated SAR data, is now correctly identified as a surface scattering element in the polarimetrically calibrated data. Fig. 17c and d show the scattering magnitudes at the dB scale for a smooth surface of the uncalibrated and calibrated S-band ISRO's LS-ASAR data. Misidentification of scattering patterns in the decomposition-based results could be easily seen in the uncalibrated data. The improvement in scattering pattern after calibration is evident in Fig. 17d

5. Discussions

From the polarimetric calibration of the ISRO's L&SBand Airborne SAR Quad-pol dataset, it was found that the crosstalk was more for the L-band dataset with a magnitude of −20.28 dB compared to the S-band dataset having a crosstalk magnitude of −30.32 dB before polarimetric calibration. For the L-band dataset, the Improved Quegan algorithm outperformed the other two algorithms reducing the crosstalk to −31.24 dB and for the S-band dataset, the Ainsworth algorithm performed the best reducing the crosstalk to −44.25 dB. Similarly, for the UAVSAR L-band dataset, the Improved Quegan algorithm gave the best performance by reducing the crosstalk from −22.49 dB to −30.85 dB.

The polarimetric calibration was also performed for the spaceborne ALOS-2 PALSAR-2 and RADARSAT-2 C-band Quad-pol datasets and as similar to the airborne Quad-pol datasets and it was noticed that the channel imbalance and phase bias polarimetric distortions were very less. For the RADARSAT-2 dataset acquired on 18th February 2019, the crosstalk before polarimetric calibration was −30.28 dB and the Ainsworth algorithm was able to minimize it to −48.35 dB. Similarly, for the dataset acquired on 14th March 2019, the crosstalk before polarimetric calibration was −28.12 dB and the Improved Quegan algorithm was able to minimize it to −46.29 dB. In

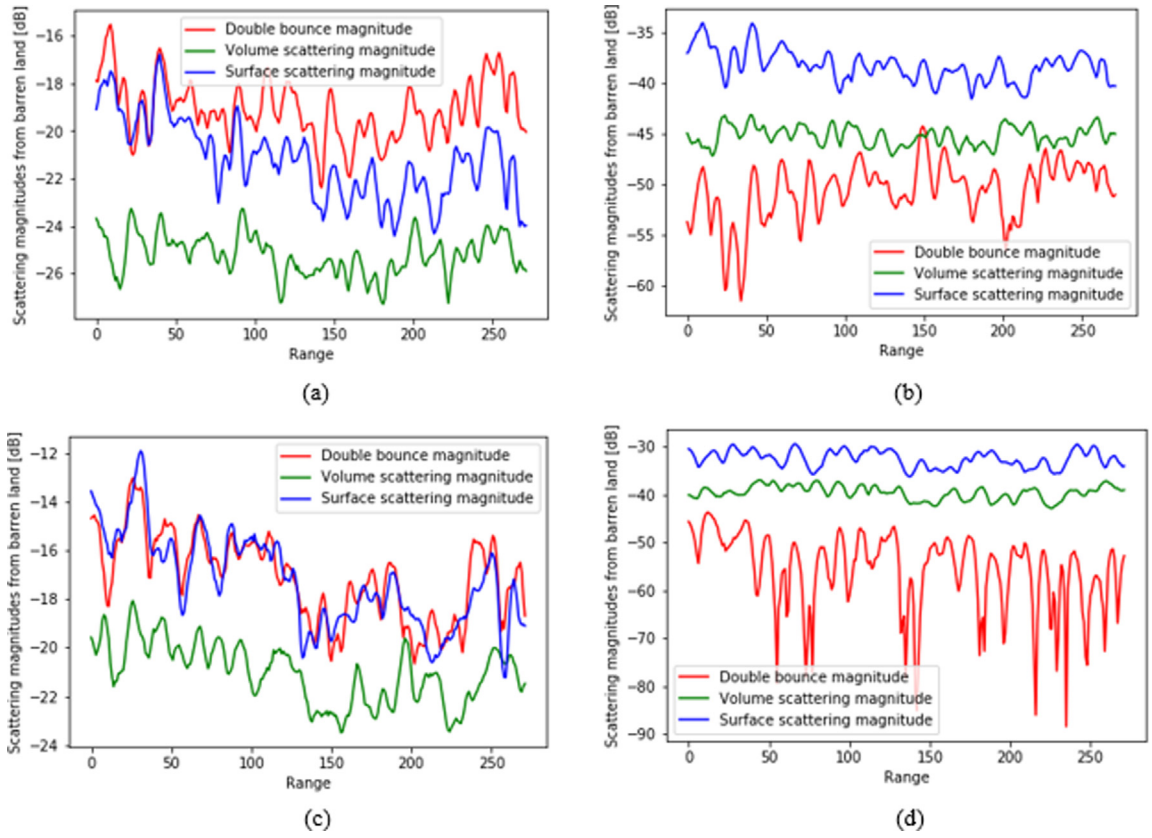

Fig. 17. The magnitude of scattering mechanisms extracted from barren land using Cloude compact-pol decomposition for ISRO's L&S Band Airborne SAR datasets; (a) L-band Airborne SAR dataset before PolCal; (b) L-band Airborne SAR dataset after PolCal; (c) S-band Airborne SAR dataset before PolCal; (d) S-band Airborne SAR dataset after PolCal.

contrast to the airborne SAR datasets, the spaceborne SAR datasets are also affected by the polarimetric distortion induced by the Earth's atmosphere. The Faraday rotation angle was estimated for the RADARSAT-2 datasets after channel imbalance, phase bias, and crosstalk calibration and it was found that the Faraday rotation angle was almost close to zero. Faraday rotation angle for the ALOS-2 PALSAR-2 of Rio Branco is nearly equal to zero. The negligible effect of ionospheric propagation of the electromagnetic wave in the L-band data is due to the study area's geographic location, which is lying near the equator and parallel to the geomagnetic line. The polarimetric distortions in the L-band ALOS-2 PALSAR-2 data due to crosstalk, channel imbalance and phase bias showed significantly smaller values than the airborne sensors. The reason behind a significantly less amount of polarimetric distortion in the ALOS-2 PALSAR-2 data may be due to the reason of already polarimetric calibration of the data by the authorised agencies before distributing it to the users.

The polarimetric signatures of the trihedral corner reflectors extracted from all the Quad-pol datasets before and after polarimetric calibration revealed that the polarimetric signatures were distorted from the ideal shapes before polarimetric calibration and after polarimetric calibration, the signatures were exactly matching with the ideal signatures. The co-polar polarimetric signatures of all the datasets were more distorted compared to the cross-polar polarimetric signatures before polarimetric calibration indicating more amount of polarimetric distortions to the co-polar HH & VV channels.

The coherency and scattering matrices analysis of the Quad-pol datasets revealed that the unexpected scattering responses observed from the ground targets before polarimetric calibration were considerably minimized after performing the polarimetric calibration and the ground targets were performing closer to their expected theoretical scattering responses. In addition, before polarimetric calibration, the cross-pol channels of the datasets were not obeying the scattering reciprocity condition (HV = VH) expected from the monostatic PolSAR systems and after polarimetric calibration, all the quad-pol datasets were perfectly obeying the scattering reciprocity constrain. The roll invariant alpha parameter analysis of the ISRO's LS Band LS-ASAR datasets showed that before polarimetric calibration, the barren lands were showing volume scattering behavior and the vegetation was showing surface scattering behavior. After polarimetric calibration, the scattering behaviors changed considerably making the barren lands to show surface scattering response and the vegetation to

show volume scattering response. There was a considerable amount of increase in double-bounce scattering that was noticed in the barren land to vegetation boundaries.

The polarimetric calibration was performed for the ISRO's L&S Band Airborne SAR compact-pol dataset and the spaceborne RISAT-1 compact-pol C-band dataset using the Freeman compact-pol polarimetric calibration algorithm. From the FRS-1 dataset of C-band RISAT-1 SAR system, it was found that the complex crosstalk parameter 'δ1′ and the channel imbalance distortion parameter 'f_1' are the most dominant polarimetric distortions. The roll invariant alpha parameter analysis showed that before polarimetric calibration, the triangular trihedral corner reflectors were showing double-bounce scattering behavior with an alpha angle of 74.38 instead of odd bounce scattering and the dihedral corner reflectors were showing odd bounce scattering behavior with an alpha angle of 11.56 instead of double-bounce scattering. After polarimetric calibration using the Freeman algorithm, the scattering response of the trihedral corner reflector changed to odd bounce scattering with an alpha value of 4.87 and the scattering response from the dihedral corner reflector changed to double bounce scattering with an alpha value of 82.97, which are expected as per the design. Similarly, the model-based Cloude compact pol decomposition revealed that there was a dominance of double bounce scattering response from barren lands and the sparsely vegetated areas were showing overestimation of volume scattering and underestimation of surface scattering. After polarimetric calibration, the barren lands were showing the dominance of surface scattering behavior. Also, minimization of the overestimation and underestimation of volume scattering and double bounce scatterings were observed in the sparsely vegetated areas respectively. A similar change in scattering behaviors was observed from the ISRO's L&S Band Airborne SAR compact-pol datasets before and after polarimetric calibration.

6. Conclusions

This study focused on the evaluating the requirement of the Polarimetric calibration for the Quad-pol and Compact-pol datasets. By performing the polarimetric calibration procedures on the ISRO's L&S Band Airborne SAR, UAVSAR L-band, ALOS-2 PALSAR-2, and RADARSAT-2 Quad-pol datasets, it was found that the channel imbalance and phase bias distortions were not high for all the datasets and the major cause for the polarimetric distortions was due to the crosstalk. Quegan, Improved Quegan, and Ainsworth methods for crosstalk calibration of quad-pol datasets were implemented in this study to assess the potential of each algorithm for the accurate estimation and minimization of the crosstalk. It was clearly understood that the Improved Quegan algorithm performs good results in a lower amount of residual crosstalk when there is very high crosstalk present in the datasets before polarimetric calibration. Ainsworth algorithm performs well to produce a dataset with a lower amount of residual crosstalk when there is low crosstalk present in the dataset before polarimetric calibration. In addition, for the lower wavelength C-band spaceborne SAR datasets, the Faraday rotation angle is close to zero indicating negligible polarimetric distortions induced due to Faraday rotation. By performing the polarimetric calibration for the compact-pol datasets using the Freeman algorithm and the polarimetric decomposition analysis using the Cloude compact-pol decomposition algorithm, it was understood that the scattering mechanisms of the ground targets were severely affected by the polarimetric distortions and after polarimetric calibration there occurred considerable improvement in the ground target characterization. From this study, it was also observed that the higher wavelength PolSAR systems are suffering from a higher amount of polarimetric distortions, especially crosstalk, and the polarimetric distortions are severely affecting the scattering mechanisms from the ground targets leading to their misinterpretation. So this study strongly recommends the consideration of the polarimetric calibration as a compulsory preprocessing step for the PolSAR datasets before using them for scientific applications.

Declaration of Competing Interest

The authors declare that they have no known competing financial interests or personal relationships that could have appeared to influence the work reported in this paper.

Acknowledgment

The Technology Development Programme (TDP) of Indian Space Research Organisation (ISRO) supported this research. The RADARSAT-2 data were purchased from the MDA corporation, ALOS-2 PALSAR-2 was procured from Remote Sensing Technology Center of Japan (RESTEC) and RISAT-1 was purchased from National Remote Sensing Centre (NRSC), ISRO, Hyderabad under the TDP. The spaceborne SAR data were procured under a TDP (code: Z1Z12PR7I601-03) on Polarimetric SAR Calibration of PolSAR Data. The authors are grateful to Shri Arun Singh Rawat, Director and Vice-Chancellor, Forest Research Institute (FRI), Dehradun, for permitting the deployment of corner reflectors in the FRI campus. The authors would like to express their gratitude to Colonel Rakesh Singh, Director, Maps Archive and Dissemination Center (MA&DC), Survey of India, Dehradun, for allowing deployment of Corner Reflectors at the Stadium of Survey of India (SoI), Dehradun. Special thanks to Dr Manoj Kumar, Scientist, FRI, Dehradun, for his scientific approach in identifying the most suitable locations for the deployment of corner reflectors in the FRI campus. The principal investigator of the project and the PolSAR calibration team is thankful to Dr Anil Kumar, Assistant Professor, University of Petroleum and Energy Studies (UPES), Dehradun, for his keen interest in identifying suit-

able locations for the deployment of corner reflectors. The authors would like to express their sincere thanks to Ms Vaishali Chaudhary, IIRS, Dehradun and Mr Rajat Garg, UPES, Dehradun, for their spontaneous contributions to the calibration exercise. The L-and S-band Airborne SAR data of ISRO were provided under NISAR L&S Airborne SAR Research Announcement (RA) of Indian Space Research Organisation (ISRO). The authors would like to express their sincere thanks to the Calibration and Validation team of Space Applications Centre (SAC), ISRO, Ahmedabad for providing the L-and S-band SAR data and sharing the corner reflector information under the NISAR L&S Band Airborne SAR Research Announcement (RA) project code Mis-01 on "Polarimetric SAR calibration of L- and S-band PolSAR data for scattering information retrieval of Manmade and Natural Features". The authors are grateful to JPL/NASA for proving the UAVSAR datasets and the information of the corner reflectors deployed at Rosamond, California. The authors are also thankful to the European Space Agency (ESA) for proving the PolSARpro v 5.0 software used for the polarimetric decomposition analysis.

References

Ainsworth, T.L., Ferro-Famil, L., Lee, J.-S., 2006. Orientation Angle Preserving A Posteriori Polarimetric SAR Calibration. IEEE Trans. Geosci. Rem. Sens. 44, 145–181. https://doi.org/10.1002/9781118116104.ch4.

Asopa, U., Kumar, S., 2020. UAVSAR Tomography for Vertical Profile Generation of Tropical Forest of Mondah National Park. Gabon. Earth Sp. Sci. 7, 1–14. https://doi.org/10.1029/2020EA001230, e2020EA001230.

Asopa, U., Kumar, S., Thakur, P.K., 2018. PSInSAR Study of Lyngenfjord Norway, using TerraSAR-X Data. In: ISPRS Annals of the Photogrammetry, Remote Sensing and Spatial Information Sciences. https://doi.org/10.5194/isprs-annals-IV-5-245-2018.

Awasthi, S., Kumar, S., Thakur, P.K., Jain, K., Kumar, A., Snehmani, 2021. Snow depth retrieval in North-Western Himalayan region using pursuit-monostatic TanDEM-X datasets applying polarimetric synthetic aperture radar interferometry based inversion Modelling. Int. J. Remote Sens. 42, 2872–2897. https://doi.org/10.1080/01431161.2020.1862439.

Awasthi, S., Kumar, S., Thakur, P.K., Mani, S., 2017. Pol-InSAR based snow depth retrieval using spaceborne TerraSAR-X data. In: 2017 8th International Conference on Computing, Communication and Networking Technologies (ICCCNT). IEEE, New Delhi, pp. 1–7. https://doi.org/10.1109/ICCCNT.2017.8204066.

Awasthi, S., Thakur, P.K., Kumar, S., Kumar, A., Jain, K., Mani, S., 2020. Snow Density retrieval using Hybrid polarimetric RISAT-1 datasets. IEEE J Sel. Top. Appl. Earth Obs. Remote Sens. 13, 3058–3065. https://doi.org/10.1109/JSTARS.2020.2991156.

Babu, A., 2019. Polarimetri Calibration of SAR data to minimise crosstalk and channel imbalance from scattering matrix. Indian Institute of Remote Sensing, Dehradun.

Babu, A., Kumar, S., 2019a. InSAR Coherence and Backscatter Images Based Analysis for the Anak Krakatau Volcano Eruption. In: Martínez-Frías, J. (Ed.), Proceedings. Multidisciplinary Digital Publishing Institute (MDPI AG). https://doi.org/10.3390/IECG2019-06216, pp. 21:1–8.

Babu, A., Kumar, S., 2019b. PSInSAR Processing for Volcanic Ground Deformation Monitoring Over Fogo Island pp. 3:1–8.. In: Martínez-Frías, J. (Ed.), Proceedings. Multidisciplinary Digital Publishing Institute (MDPI AG). https://doi.org/10.3390/IECG2019-06217.

Babu, A., Kumar, S., 2019c. SBAS interferometric analysis for volcanic eruption of Hawaii island. J. Volcanol. Geoth. Res. 370, 31–50. https://doi.org/10.1016/j.jvolgeores.2019.01.011.

Babu, A., Kumar, S., Agrawal, S., 2020. Polarimetric Calibration of L-Band UAVSAR Data. J. Indian Soc. Remote Sens. https://doi.org/10.1007/s12524-020-01241-1.

Babu, A., Kumar, S., Agrawal, S., 2019a. Polarimetric Calibration of RISAT-1 Compact-Pol Data. IEEE J. Sel. Top. Appl. Earth Obs. Remote Sens. 12, 3731–3736. https://doi.org/10.1109/JSTARS.2019.2932019.

Babu, Arun, Kumar, S., Agrawal, S., 2019. RISAT-1 Compact Polarimetric Calibration and Decomposition. Proceedings 18, 6189. https://doi.org/10.3390/ECRS-3-06189

Balss, U., Gisinger, C., Eineder, M., Breit, H., Schubert, A., Small, D., 2018. Survey Protocol for Geometric SAR Sensor Analysis. Oberpfaffenhofen.

Bamler, R., Hartl, P., 1998. Synthetic aperture radar interferometry. Inverse Probl. 14, R1. https://doi.org/10.1088/0266-5611/14/4/001.

Behera, M.D., Tripathi, P., Mishra, B., Kumar, S., Chitale, V.S., Behera, S.K., 2016. Above-ground biomass and carbon estimates of Shorea robusta and Tectona grandis forests using QuadPOL ALOS PALSAR data. Adv. Sp. Res. 57, 552–561. https://doi.org/10.1016/j.asr.2015.11.010.

Bhanu Prakash, M.E., Kumar, S., 2021. PolInSAR decorrelation-based decomposition modelling of spaceborne multifrequency SAR data. Int. J. Remote Sens. 42, 1398–1419. https://doi.org/10.1080/01431161.2020.1829155.

Bickel, S., Bates, R.H., 1965. Effects of Magneto-Ionic Propagation on the Polarization Scattering Matrix. In: Proceedings of the IEEE. https://doi.org/10.1109/PROC.1965.4097.

Brunfeldt, D.R., Ulaby, F.T., 1984. Active Reflector for Radar Calibration. IEEE Trans. Geosci. Remote Sens. GE-22, 165–169. https://doi.org/10.1109/TGRS.1984.350610.

Buchhorn, M., Smets, B., Bertels, L., Roo, B. De, Lesiv, M., Tsendbazar, N.-E., Herold, M., Fritz, S., 2020a. Copernicus Global Land Service: Land Cover 100m: collection 3: epoch 2019: Globe [WWW Document]. Copernicus L. Monit. Serv. https://doi.org/10.5281/ZENODO.3939050.

Buchhorn, M., Smets, B., Bertels, L., Roo, B. De, Lesiv, M., Tsendbazar, N.-E., Li, L., Tarko, A., 2020b. Copernicus Global Land Service: Land Cover 100m: Version 3 Globe 2015-2019: Product User Manual, I3.3. ed, Copernicus Global Land Operations. Copernicus Global Land Operations, Zenodo, Geneve, Switzerland. https://doi.org/10.5281/zenodo.3938963.

Carter, D.J.Q., Hurd, D.L., Cordey, R.A., 1997. Calibration and characterisation of spaceborne Synthetic Aperture Radars (SAR). Adv. Sp. Res. 19, 1415–1423. https://doi.org/10.1016/S0273-1177(97)00255-X.

Chandni, C.K., Kumar, S., 2020. DInSAR based analysis of January 2020 eruption of Fernandina volcano, Galapagos. In: IEEE International India Geoscience and Remote Sensing Symposium 2020. IEEE, Ahmedabad, pp. 1–4.

Chang, Y., Li, P., Yang, J., Zhao, J., Zhao, L., Shi, L., 2018. Polarimetric calibration and quality assessment of the GF-3 satellite images. Sensors (Switzerland) 18, 1–12. https://doi.org/10.3390/s18020403.

Chapman, B., Siqueira, P., Saatchi, S., Simard, M., Kellndorfer, J., 2019. Initial results from the 2019 NISAR Ecosystem Cal/Val Exercise in the SE USA. In: 2019 IEEE International Geoscience and Remote Sensing Symposium (IGARSS 2019), IEEE International Symposium on Geoscience and Remote Sensing IGARSS, pp. 8641–8644.

Chaudhary, V., Kumar, S., 2020. Marine Oil Slicks Detection using Spaceborne and Airborne SAR data. Adv. Sp. Res. 66, 854–872. https://doi.org/10.1016/j.asr.2020.05.003.

Chen, J., Quegan, S., 2011. Calibration of spaceborne CTLR compact polarimetric low-frequency SAR using mixed radar calibrators. IEEE

Trans. Geosci. Remote Sens. 49, 2712–2723. https://doi.org/10.1109/TGRS.2011.2109065.

Chorowicz, J., Dhont, D., Gündogdu, N., 1999. Neotectonics in the eastern North Anatolian fault region (Turkey) advocates crustal extension: Mapping from SAR ERS imagery and Digital Elevation Model. J. Struct. Geol. 21, 511–532. https://doi.org/10.1016/S0191-8141(99)00022-X.

Das, A.K., Kumar, R., Ramanujam, V.M., Bham, R., 2019. Application Potential of L&S band Airborne SAR developed as a Pre-cursor to the Space-borne NISAR Mission. In: 2019 URSI ASIA-PACIFIC RADIO SCIENCE CONFERENCE (AP-RASC).

ESA, 2014. PALSAR-IPF SAR Data Products Product Handbook.

Falk, A., Gerald, B., Adrian, B., Sean, B., Susan, C., Manab, C., Bruce, C., Anup, D., Andrea, D., Ralph, D., Kurt, F., Eric, F., Richard, F., Margaret, G., Bradford, H., Scott, H., Benjamin, H., Cathleen, J., Ian, J., Josef, K., Raj, K., Rowena, L., Zhong, L., Franz, M., Tapan, M., Frank, M., Sandip, O., Matthew, P., Eric, R., Paul, R., Sassan, S., Priyanka, S., Marc, S., Mark, S., Paul, S., Howard, Z., 2018. NASA-ISRO SAR (NISAR) Mission Science Users ' Handbook, first ed. Jet Propulsion Laboratory, California Institute of Technology, California.

Ferrer, P.J., López-Martínez, C., Aguasca, A., Pipia, L., González-Arbesú, J.M., Fabregas, X., Romeu, J., 2011. Transpolarizing trihedral corner reflector characterization using a GB-SAR system. IEEE Geosci. Remote Sens. Lett. 8, 774–778. https://doi.org/10.1109/LGRS.2011.2113313.

Fore, A.G., Chapman, B.D., Hawkins, B.P., Hensley, S., Jones, C.E., Michel, T.R., Muellerschoen, R.J., 2015. UAVSAR Polarimetric Calibration. IEEE Trans. Geosci. Remote Sens. 53, 3481–3491. https://doi.org/10.1109/TGRS.2014.2377637.

Freeman, A., 1992. SAR Calibration: An Overview. IEEE Trans. Geosci. Remote Sens. 30, 1107–1121. https://doi.org/10.1109/36.193786.

Freeman, A., Curlander, J.C., 1989. Radiometric correction and calibration of SAR images. Photogramm. Eng. Remote Sens. 55, 1295–1301.

Freeman, A., Dubois-Fernandez, P., Truong-Loi, M., 2008. Compact Polarimetry at longer wavelengths - calibration. In: 7th European Conference on Synthetic Aperture Radar, pp. 1–4.

Freeman, A., Durden, S.L., 1998. A three-component scattering model for polarimetric SAR data. IEEE Trans. Geosci. Remote Sens. 36, 963–973. https://doi.org/10.1109/36.673687.

Freeman, A., Shen, Y., Werner, C.L., 1990. Polarimetric SAR Calibration Experiment Using Active Radar Calibrators. IEEE Trans. Geosci. Remote Sens. 28, 224–240. https://doi.org/10.1109/36.46702.

Fujita, M., Masuda, T., Fujino, Y., 1998. Polarimetric calibration of the SIR-C C-band channel using active radar calibrators and polarization selective dihedrals. IEEE Trans. Geosci. Remote Sens. 36, 1872–1878. https://doi.org/10.1109/36.729358.

Garthwaite, M.C., Nancarrow, S., Hislop, A., Thankappan, M., Dawson, J.H., Lawrie, S., 2015. The Design of Radar Corner Reflectors for the Australian Geophysical Observing System: a single design suitable for InSAR deformation monitoring and SAR calibration at multiple microwave frequency bands. Canberra. https://doi.org/10.11636/Record.2015.003.

Goldstein, R.M., Werner, C.L., 1998. Radar interferogram filtering for geophysical applications. Geophys. Res. Lett. 25, 4035. https://doi.org/10.1029/1998GL900033.

Gong, Y., Wanga, R., Li, N., Wang, P., Xu, Z., Leng, Y., 2017. A polarimetric SAR internal calibration scheme for polarization cross-talk. Remote Sens. Lett. 8, 879–887. https://doi.org/10.1080/2150704X.2017.1332796.

Gonnuru, P., Kumar, S., 2018. PsInSAR based land subsidence estimation of Burgan oil field using TerraSAR-X data. Remote Sens. Appl.: Soc. Environ. 9, 17–25. https://doi.org/10.1016/j.rsase.2017.11.003.

Gosselin, G., Touzi, R., Cavayas, F., 2014. Polarimetric Radarsat-2 wetland classification using the Touzi decomposition: case of the Lac Saint-Pierre Ramsar wetland. Can. J. Remote Sens. 39, 491–506. https://doi.org/10.5589/m14-002.

Grover, A., Kumar, S., Kumar, A., 2018. Ship detection using sentinel-1 SAR data. ISPRS Ann. Photogram. Remote Sens. Spatial Inform. Sci., 317–324 https://doi.org/10.5194/isprs-annals-IV-5-317-2018.

IDEAS SAR Team, 2009. ADEN AlOS PALSAR Cyclic Report: 25 January 2009 to 12 March 2009, Technical Note. Frascati, Italy.

Jayasri, P.V., Niharika, K., Joseph, M., Usha Sundari Ryali, H.S.V., Ramana Sarma, C.V., Sita Kumari, E.V.S., Prasad, A.V.V., 2018. Implementation of RISAT-1 Hybrid Polarimetric Decomposition Techniques and Analysis Using Corner Reflector Data. J. Indian Soc. Remote Sens. 46, 1005–1012. https://doi.org/10.1007/s12524-018-0758-2.

Joshi, S.K., Kumar, S., 2017. Spaceborne PolInSAR tomography for vertical profile retrieval of forest vegetation. J. Appl. Remote Sens. 11. https://doi.org/10.1117/1.jrs.11.016001 016001.

Joshi, S.K., Kumar, S., Agrawal, S., Dinh, H.T.M., 2016. PolInSAR tomography for vertical profile retrieval of forest vegetation using spaceborne SAR data. In: Land Surface and Cryosphere Remote Sensing III. SPIE, New Delhi, p. 987709. https://doi.org/10.1117/12.2228068.

Kellogg, K., Hoffman, P., Standley, S., Shaffer, S., Rosen, P., Edelstein, W., Dunn, C., Baker, C., Barela, P., Shen, Y., Guerrero, A.M., Xaypraseuth, P., Sagi, V.R., Sreekantha, C.V., Harinath, N., Kumar, R., Bhan, R., Sarma, C.V.H.S., 2020. NASA-ISRO Synthetic Aperture Radar (NISAR) Mission. In: in: 2020 IEEE Aerospace Conference, pp. 1–21. https://doi.org/10.1109/AERO47225.2020.9172638.

Kimura, H., Mizuno, T., Papathanassiou, K.P., Hajnsek, I., 2004. Improvement of polarimetric SAR calibration based on the Quegan algorithm. IGARSS 2004. 2004 IEEE Int. Geosci. Remote Sens. Symp., vol. 1, pp. 184–187. https://doi.org/10.1109/igarss.2004.1368990.

Kumar, S., 2019. PolInSAR and PolTomSAR based modelling for characterization of forest parameters. Indian Institute of Technology, Roorkee.

Kumar, S., Garg, R.D., Govil, H., Kushwaha, S.P.S., 2019. PolSAR-decomposition-based extended water cloud modeling for forest aboveground biomass estimation. Remote Sens. 11, 1–27. https://doi.org/10.3390/rs11192287.

Kumar, S., Garg, R.D., Kushwaha, S.P.S., 2016a. Deorientation of PolSAR coherency matrix for volume scattering retrieval. In: Proc. SPIE 9877, Land Surface and Cryosphere Remote Sensing III. Spie-Int Soc Optical Engineering, Delhi, pp. 987705–987718. https://doi.org/10.1117/12.2223680.

Kumar, S., Garg, R.D., Kushwaha, S.P.S., Pandey, U., 2017a. Spaceborne SAR Tomography for Vertical Profile Retrieval of Forest Vegetation. Proc. Natl. Acad. Sci. India Sect. A - Phys. Sci. 87, 807–816. https://doi.org/10.1007/s40010-017-0450-x.

Kumar, S., Govil, H., Srivastava, P.K., Thakur, P.K., Kushwaha, S.P.S., 2020a. Spaceborne Multifrequency PolInSAR-Based Inversion Modelling for Forest Height Retrieval. Remote Sens. 12, 1–27. https://doi.org/10.3390/rs12244042.

Kumar, S., Joshi, S.K., 2017. SAR tomography for forest structure investigation. In: Asia-Pacific Microwave Conference Proceedings, APMC. IEEE, pp. 1–4. https://doi.org/10.1109/APMC.2016.7931452.

Kumar, S., Joshi, S.K., Govil, H., 2017b. Spaceborne PolSAR tomography for forest height retrieval. IEEE J. Sel. Top. Appl. Earth Obs. Remote Sens. 10, 5175–5185. https://doi.org/10.1109/JSTARS.2017.2741723.

Kumar, S., Joshi, S.K., Tomar, K.S., Aggarwal, N., Khati, U.G., Chandola, S., Sai Bharadwaj, P., Agarwal, S., Kushwaha, S.P.S., 2017c. PolInSAR based modelling for scattering characterization and forest parameter retrieval. In: The 38th Asian Conference on Remote Sensing, ACRS 2017, Space Applications: Touching Human Lives. Asian Association on Remote Sensing (AARS), New Delhi, pp. 1–10.

Kumar, S., Kandasamy, V.S., Babu, A., Thakur, P.K., Agrawal, S., 2020b. PSInSAR-based Surface Deformation Mapping of Angkor Wat Cultural Heritage Site. J. Indian Soc. Remote Sens. 1–16. https://doi.org/10.1007/s12524-020-01257-7.

Kumar, S., Kattamuri, H.P., Agarwal, S., 2016b. Dark spot detection for characterization of marine surface slicks using PolSAR remote sensing. In: Remote Sensing of the Oceans and Inland Waters: Techniques, Applications, and Challenges. SPIE, New Delhi, p. 98780K. https://doi.org/10.1117/12.2224415.

Kumar, S., Khati, U.G., Chandola, S., Agrawal, S., Kushwaha, S.P.S., 2017d. Polarimetric SAR Interferometry based modeling for tree height and aboveground biomass retrieval in a tropical deciduous forest. Adv. Sp. Res. 60, 571–586. https://doi.org/10.1016/j.asr.2017.04.018.

Kumar, S., Kumari, V., Alice, A., M.E.B.P., Babu, A., Maiti, A., Agrawal, S., 2020c. Polarimetric SAR calibration and processing tool V1.0: A tool for polarimetric calibration and processing of SAR data. In: 2020 7th International Conference on Signal Processing and Integrated Networks, SPIN 2020, pp. 459–464. https://doi.org/10.1109/SPIN48934.2020.9071299.

Kumar, S., Pandey, U., Kushwaha, S.P., Chatterjee, R.S., Bijker, W., 2012. Aboveground biomass estimation of tropical forest from Envisat advanced synthetic aperture radar data using modeling approach. J. Appl. Remote Sens. 6. https://doi.org/10.1117/1.JRS.6.063588 063588.

Labrière, N., Tao, S., Chave, J., Scipal, K., Toan, T.L., Abernethy, K., Alonso, A., Barbier, N., Bissiengou, P., Casal, T., Davies, S.J., Ferraz, A., Hérault, B., Jaouen, G., Jeffery, K.J., Kenfack, D., Korte, L., Lewis, S.L., Malhi, Y., Memiaghe, H.R., Poulsen, J.R., Réjou-Méchain, M., Villard, L., Vincent, G., White, L.J.T., Saatchi, S., 2018. In Situ Reference Datasets From the TropiSAR and AfriSAR Campaigns in Support of Upcoming Spaceborne Biomass Missions. IEEE J. Sel. Top. Appl. Earth Obs. Remote Sens. 11, 3617–3627. https://doi.org/10.1109/JSTARS.2018.2851606.

Lee, J.S., Pottier, E., 2017. Polarimetric radar imaging: From basics to applications, Polarimetric Radar Imaging: From Basics to Applications. https://doi.org/10.1201/9781420054989.

Lenz, R., Schuler, K., Younis, M., Wiesbeck, W., 2006. TerraSAR-X active radar ground calibrator system. IEEE Aerosp. Electron. Syst. Mag. 21, 30–33. https://doi.org/10.1109/MAES.2006.1635172.

Li, J., Ji, Y., Zhang, Y., Zhang, Q., Huang, H., Dong, Z., 2018. A Novel Strategy of Ambiguity Correction for the Improved Faraday Rotation Estimator in Linearly Full-Polarimetric SAR Data. Sensors 18, 1158. https://doi.org/10.3390/s18041158.

Li, L., Hong, J., Ming, F., Liang, W.-B., 2012. An approach for ionospheric effects correction on spaceborne SAR calibration based on active radar calibrator. Dianzi Yu Xinxi Xuebao/J. Electron. Inf. Technol. 34, 1096–1101. https://doi.org/10.3724/SP.J.1146.2011.00978.

Liang, W., Jia, Z., Hong, J., Zhang, Q., Wang, A., Deng, Z., 2020. Polarimetric Calibration Scheme Combining Internal and External Calibrations, and Experiment for Gaofen-3. IEEE Access 8, 7659–7671. https://doi.org/10.1109/ACCESS.2020.2963937.

Livingstone, C.E., Sikaneta, I., Gierull, C., Chiu, S., Beaulne, P., 2015. RADARSAT-2 System and Mode Description. Ottawa.

Maiti, A., 2019. Polarimetric Calibration of Sar Data Using Manmade Point Targets and Uniformly Distributed Natural Targets. Faculty Geo-Information Science and Earth Observation (ITC), University of Twente.

Maiti, A., Kumar, S., Tolpekin, V.A., Agarwal, S., 2021. A Computationally Efficient Hybrid Framework for Polarimetric Calibration of Quad-Pol SAR Data. Earth Sp. Sci. 1–20. https://doi.org/10.1029/2020EA001447.

Majumdar, S., Thakur, P.K., Chang, L., Kumar, S., Smith, R.G., 2019a. Spaceborne Polarimetric SAR Interferometry for Snow Depth Retrieval in the Northwestern Himalayan Watershed. In: 2019 Geological Society of America (GSA) Annual Meeting. Phoenix, Arizona, USA. https://doi.org/10.1130/abs/2019AM-338916.

Majumdar, S., Thakur, P.K., Ling, C., Kumar, S., 2019b. X-band Polarimetric SAR Copolar Phase Difference for Fresh Snow Depth Estimation in the Northwestern Himalayan Watershed. In: IEEE 2019 International Geoscience and Remote Sensing Symposium (IGARSS 2019). IEEE, Yokohama, Japan, pp. 4104–4105.

Mangla, R., Kumar, S., 2014. DEM Construction using DInSAR. ISPRS – Int. Arch. Photogramm. Remote Sens. Spatial Inform. Sci., 817–820 https://doi.org/10.5194/isprsarchives-XL-8-817-2014.

Massonnet, D., Rossi, M., Carmona, C., Adragna, F., Peltzer, G., Feigl, K., Rabaute, T., 1993. The displacement field of the Landers earthquake mapped by radar interferometry. Nature 364, 138–142. https://doi.org/10.1038/364138a0.

McElfresh, S.B.Z., Harbert, W., Ku, C.-Y., Lin, J.-S., 2002. Stress modeling of tectonic blocks at Cape Kamchatka, Russia using principal stress proxies from high-resolution SAR: New evidence for the Komandorskiy Block. Tectonophysics 354, 239–256. https://doi.org/10.1016/S0040-1951(02)00341-4.

Mohr, J.J., Madsen, S.N., 2001. Geometric calibration of ERS Satellite SAR images. IEEE Trans. Geosci. Remote Sens. 39, 842–850. https://doi.org/10.1109/36.917909.

Moreira, A., Bachmann, M., Balzer, W., Tridon, D.B., Diedrich, E., Fritz, T., Grigorov, C., Kahle, R., Krieger, G., Hajnsek, I., Huber, S., Jörg, H., Klenk, P., Lachaise, M., Maier, M., Maurer, E., Papathanassiou, K., Parizzi, A., Prats, P., Reimann, J., Rodriguez, M., Schättler, B., Schwinger, M., Schulze, D., Steinbrecher, U., Villano, M., Younis, M., Zan, F. De, Zink, M., Zonno, M., 2018. Tandem-L: Project Status and Main Findings of the Phase Bl Study. In: IGARSS 2018 - 2018 IEEE International Geoscience and Remote Sensing Symposium. pp. 8667–8670. https://doi.org/10.1109/IGARSS.2018.8518591

Moreira, A., Prats-iraola, P., Younis, M., Krieger, G., Hajnsek, I., Papathanassiou, K.P., 2013. A tutorial on synthetic aperture radar. IEEE Geosci. Remote Sens. Mag. 1, 6–43. https://doi.org/10.1109/MGRS.2013.2248301.

Moriyama, T., 2015. Polarimetric calibration of PALSAR2. In: 2015 IEEE Int. Geosci. Remote Sens. Symp. 1284–1287. https://doi.org/10.1109/IGARSS.2015.7326009.

Moriyama, T., Shimada, M., Tadono, T., 2007. Polarimetric Calibration of ALOS / PALSAR. In: ISAP, pp. 776–779.

Muellerschoen, R., 2020. Calibration [WWW Document]. Technology. URL https://uavsar.jpl.nasa.gov/cgi-bin/calibration.pl (accessed 1.6.21).

Navarro, A., Lourenço, N., Chorowicz, J., Miranda, J.M., Catalão, J., 2009. Analysis of geometry of volcanoes and faults in Terceira Island (Azores): Evidence for reactivation tectonics at the EUR/AFR plate boundary in the Azores triple junction. Tectonophysics 465, 98–113. https://doi.org/10.1016/j.tecto.2008.10.020.

Ouchi, K., 2013. Recent trend and advance of synthetic aperture radar with selected topics. Remote Sens. https://doi.org/10.3390/rs5020716.

Pottier, E., Ferro-Famil, L., 2012. PolSARPro V5.0: An ESA educational toolbox used for self-education in the field of POLSAR and POLINSAR data analysis. In: International Geoscience and Remote Sensing Symposium (IGARSS), pp. 7377–7380. https://doi.org/10.1109/IGARSS.2012.6351925.

Pottier, E., Ferro-Famil, L., Allain, S., Cloude, S., Hajnsek, I., Papathanassiou, K., Moreira, A., Williams, M., Minchella, A., Lavalle, M., Desnos, Y.-L., 2009. Overview of the PolSARpro v4.0 Software. The open source toolbox for polarimetric and interferometric polarimetric SAR data processing. In: International Geoscience and Remote Sensing Symposium (IGARSS), pp. 936–939. https://doi.org/10.1109/IGARSS.2009.5417532.

Quegan, S., 1994. A Unified Algorithm for Phase and Cross-Talk Calibration of Polarimetric Data-Theory and Observations. IEEE Trans. Geosci. Remote Sens. 32, 89–99. https://doi.org/10.1109/36.285192.

Rabus, B., Eineder, M., Roth, A., Bamler, R., 2003. The shuttle radar topography mission - A new class of digital elevation models acquired by spaceborne radar. ISPRS J. Photogramm. Remote Sens. 57, 241–262. https://doi.org/10.1016/S0924-2716(02)00124-7.

Raney, R.K., 2007. Hybrid-Polarity SAR Architecture. IEEE Trans. Geosci. Remote Sens. 45, 3397–3404. https://doi.org/10.1016/0014-4827(56)90188-4.

Rao, Y.S., Kumar, V., 2017. Hybrid Polarimetric RISAT-1 SAR Data Evaluation using Corner Reflectors. In: Calibration and Validation for SAR Systems: Workshop 2017. The Committee on Earth Observation Satellites Working Group on Calibration and Validation Synthetic Aperture Radar Subgroup, Pasadena, Los Angeles, California, United States of America, pp. 1–33.

Reimann, J., Schwerdt, M., Schmidt, K., Ramon, N.T., Döring, B., 2017. The DLR Spaceborne SAR Calibration Center. Frequenz 71, 619–627. https://doi.org/10.1515/freq-2016-0274.

Rosen, P.A., 2000. Synthetic aperture radar interferometry. Proc. IEEE 88, 333–380. https://doi.org/10.1109/5.838084.

Sai Bharadwaj, P., Kumar, S., Kushwaha, S.P.S., Bijker, W., 2015. Polarimetric scattering model for estimation of above ground biomass of multilayer vegetation using ALOS-PALSAR quad-pol data. Phys. Chem. Earth. 83–84, 187–195. https://doi.org/10.1016/j.pce.2015.09.003.

Sarabandi, K., Oh, Y., Ulaby, F.T., 1992a. Performance Characterization of Polarimetric Active Radar Calibrators and a New Single Antenna Design. IEEE Trans. Antennas Propag. 40, 1147–1154. https://doi.org/10.1109/8.182446.

Sarabandi, K., Pierce, L.E., Dobson, M.C., Ulaby, F.T., Stiles, J.M., Chiu, T.C., De Roo, R., Hartikka, R., Zambetti, A., 1995. Polarimetric Calibration of SIR-C Using Point and Distributed Targets. IEEE Trans. Geosci. Remote Sens. 33, 858–866. https://doi.org/10.1109/36.406672.

Sarabandi, K., Pierce, L.E., Ulaby, F.T., 1992b. Calibration of a Polarimetric Imaging SAR. IEEE Trans. Geosci. Remote Sens. 30, 540–549. https://doi.org/10.1109/36.142932.

Schubert, A., Small, D., Miranda, N., Geudtner, D., Meier, E., 2015. Sentinel-1A product geolocation accuracy: Commissioning phase results. Remote Sens. 7, 9431–9449. https://doi.org/10.3390/rs70709431.

Schubert, A.A., Small, D., Gisinger, C., 2017. Corner Reflector Deployment for SAR Geometric Calibration and Performance Assessment. Zurich, Switzerland.

Schwerdt, M., Schmidt, K., Ramon, N.T., Klenk, P., Yague-Martinez, N., Prats-Iraola, P., Zink, M., Geudtner, D., 2017. Independent system calibration of sentinel-1B. Remote Sens. 9. https://doi.org/10.3390/rs9060511.

Seifert, F.M., Zink, M., Kietzmann, H., Blötscher, H., 1996. Calibration and performance analysis of the X-SAR system. Adv. Sp. Res. 17, 71–74. https://doi.org/10.1016/0273-1177(95)00450-S.

Shafai, S.S., Kumar, S., 2020. PolInSAR Coherence and Entropy-Based Hybrid Decomposition Model. Earth Sp. Sci. 7, 1–17. https://doi.org/10.1029/2020ea001279, e2020EA001279.

Sharma, S., Dadhich, G., Rambhia, M., Mathur, A.K., Prajapati, R.P., Patel, P.R., Shukla, A., 2017. Radiometric calibration stability assessment for the RISAT-1 SAR sensor using a deployed point target array at the Desalpar site, Rann of Kutch. India. Int. J. Remote Sens. 38, 7242–7259. https://doi.org/10.1080/01431161.2017.1371858.

Sheen, D.R., Johansen, E.L., Elenbogen, L.P., Kasischke, E.S., 1992. The Gridded Trihedral: A New Polarimetric Sar Calibration Reflector. IEEE Trans. Geosci. Remote Sens. 30, 1149–1153. https://doi.org/10.1109/36.193791.

Shi, L., Li, P., Yang, J., Zhang, L., Ding, X., Zhao, L., 2020. Polarimetric SAR Calibration and Residual Error Estimation When Corner Reflectors Are Unavailable. IEEE Trans. Geosci. Remote Sens. 58, 4454–4471. https://doi.org/10.1109/TGRS.2020.2964732.

Shimada, M., 2019. Imaging from Spaceborne and Airborne SARs, Calibration, and Applications. Taylor & Francis Group, LLC.

Shimada, M., 1996. Radiometric and geometric calibration of JERS-1 SAR. Adv. Sp. Res. 17, 79–88. https://doi.org/10.1016/0273-1177(95)00452-K.

Shimada, M., Isoguchi, O., Tadono, T., Isono, K., 2009. PALSAR Radiometric and Geometric Calibration. IEEE Trans. Geosci. Remote Sens. 47, 3915–3932. https://doi.org/10.1109/TGRS.2009.2023909.

Shimada, M., Oaku, H., Nakai, M., 1999. SAR calibration using frequency-tunable active radar calibrators. IEEE Trans. Geosci. Remote Sens. 37, 564–573. https://doi.org/10.1109/36.739116.

Shukla, S., Kumar, S., Tolpekin, V.A., 2019. Petrophysical Insights Into Lunar Mafic Extrusive Basalts Over Reiner Gamma Formation. IEEE J. Sel. Top. Appl. Earth Obs. Remote Sens. PP, 1–17. https://doi.org/10.1109/jstars.2019.2909352.

Shukla, Shashwat, Maiti, A., Patterson, G.W., Prem, P., Cahill, J.T.S., Thomson, B.J., Tolpekin, V.A., Kumar, S., 2020a. Mini-RF Global and Polar S-Band Maps of the Variation in the Moon's Dielectric Constant. In: 51st Lunar and Planetary Science Conference (2020). The Woodlands, Texas, USA, p. 2509.

Shukla, S., Tolpekin, V., Kumar, S., Stein, A., 2020b. Investigating the retention of solar wind implanted helium-3 on the moon from the analysis of multi-wavelength remote sensing data. Remote Sens. 12. https://doi.org/10.3390/rs12203350.

Singh, A., Gaurav, K., Meena, G.K., Kumar, S., 2020. Estimation of Soil Moisture Applying Modified Dubois Model to Sentinel-1; A Regional Study from Central India. Remote Sens. 12, 2266-1-19.

Space Applications Centre, 2016. Research Announcement for L&S band Airborne SAR. Ahmedabad.

Srivastava, S.K., Cote, S., Le Dantec, P., Hawkins, R.K., Murnaghan, K., 2007. RADARSAT-1 calibration and image quality evolution to the extended mission. Adv. Sp. Res. 39, 7–12. https://doi.org/10.1016/j.asr.2006.02.027.

Srivastava, S.K., Hawkins, R.K., Banik, B.T., Adamovic, M., Gray, R., Murnaghan, K., Lukowski, T.I., Jefferies, W.C., 2001. RADARSAT-1 image quality and calibration — a continuing success. Adv. Sp. Res. 28, 99–108. https://doi.org/10.1016/S0273-1177(01)00305-2.

Srivastava, S.K., Hawkins, R.K., Lukowski, T.I., Banik, B.T., Adamovic, M., Jefferies, W.C., 1999. RADARSAT image quality and calibration — Update. Adv. Sp. Res. 23, 1487–1496. https://doi.org/10.1016/S0273-1177(99)00302-6.

Srivastava, S.K., Le Dantec, P., Hawkins, R.K., Banik, B.T., Gray, R., Murnaghan, K., Guertin, G., Shepherd, N., 2003. RADARSAT-1 image quality and calibration — Continuing success in extended mission. Adv. Sp. Res. 32, 2295–2304. https://doi.org/10.1016/S0273-1177(03)90557-6.

Srivastava, S.K., Lukowski, T.I., Gray, R.B., Shepherd, N.W., Banik, B., Hawkins, R.K., Cloutier, C., 1997. Calibration and image quality performance results of RADARSAT. Adv. Sp. Res. 19, 1447–1454. https://doi.org/10.1016/S0273-1177(97)00259-7.

Srivastava, S.K., Shepherd, N.W., Lukowski, T.I., Hawkins, R.K., 1996. Plans for RADARSAT image data calibration. Adv. Sp. Res. 17, 89–96. https://doi.org/10.1016/0273-1177(95)00453-L.

Sun, G., Huang, L., Chen, K., Han, C., 2017. An Efficient Polarimetric SAR Calibration Algorithm Using Corner Reflectors. Can. J. Remote Sens. 43, 286–296. https://doi.org/10.1080/07038992.2017.1330142.

Tan, H., Hong, J., 2016. Calibration of Compact Polarimetric SAR Images Using Distributed Targets and One Corner Reflector. IEEE Trans. Geosci. Remote Sens. 54, 4433–4444. https://doi.org/10.1109/TGRS.2016.2541666.

Tan, H., Hong, J., 2015. Correction of transmit crosstalk in reconstruction of quad-pol data from compact polarimetry data. IEEE Geosci. Remote Sens. Lett. 12, 1051–1055. https://doi.org/10.1109/LGRS.2014.2377491.

Toan, T.L., Chave, J., Dall, J., Papathanassiou, K., Paillou, P., Rechstein, M., Quegan, S., Saatchi, S., Seipel, K., Shugart, H., Tebaldini, S., Ulander, L., Williams, M., 2018. The Biomass Mission: Objectives and Requirements. In: IGARSS 2018 - 2018 IEEE International Geoscience and Remote Sensing Symposium. pp. 8563–8566. https://doi.org/10.1109/IGARSS.2018.8518491.

Touzi, R., 2017. The Touzi decomposition for a unique target scattering characterization using polarimetric SAR. In: 38th Asian Conference on Remote Sensing - Space Applications: Touching Human Lives, ACRS 2017. Asian Association on Remote Sensing (AARS), New Delhi, India, pp. 1–5.

Touzi, R., 2009. Compact-Hybrid versus Linear- Dual and Fully Polarimetric SAR. In: Lacoste, H., Ouwehand, L. (Eds.), Proceedings of the Fourth International Workshop on Science and Applications of SAR Polarimetry and Polarimetric Interferometry PolInSAR 2009. European Space Agency, Noordwijk, Netherlands, pp. 26–30.

Touzi, R., 2007. Target scattering decomposition in terms of roll-invariant target parameters. IEEE Trans. Geosci. Remote Sens. 45, 73–84. https://doi.org/10.1109/TGRS.2006.886176.

Touzi, R., Deschamps, A., Rother, G., 2009. Phase of Target Scattering for Wetland Characterization Using Polarimetric C-Band SAR. IEEE Trans. Geosci. Remote Sens. 47, 3241–3261. https://doi.org/10.1109/TGRS.2009.2018626.

Touzi, R., Hawkins, R.K., Cote, S., 2013. High-precision assessment and calibration of polarimetric RADARSAT-2 SAR using transponder measurements. IEEE Trans. Geosci. Remote Sens. 51, 487–503. https://doi.org/10.1109/TGRS.2012.2201946.

Tridon, D.B., Sica, F., Zan, F. De, Bachmann, M., Krieger, G., 2018. Observation Strategy and Flight Configuration for Monitoring Earth Dynamics with the Tandem-L Mission. In: IGARSS 2018–2018 IEEE International Geoscience and Remote Sensing Symposium, pp. 5651–5654. https://doi.org/10.1109/IGARSS.2018.8517757.

Truong-Loï, M.L., Dubois-Fernandez, P., Pottier, E., Freeman, A., Souyris, J.C., 2010. Potentials of a compact polarimetric SAR system. Int. Geosci. Remote Sens. Symp. 742–745. https://doi.org/10.1109/IGARSS.2010.5649036.

Ulander, L.M.H., 1996. Radiometrie slope correction of synthetic-aperture radar images. IEEE Trans. Geosci. Remote Sens. 34, 1115–1122. https://doi.org/10.1109/36.536527.

Upadhyay, A., 2021a. Brazil Shapefile download free – Country Boundary, Polygon, states map [WWW Document]. IGIS Map. URL https://map.igismap.com/gis-data/brazil/administrative_boundaries_national_polygon (accessed 1.5.21).

Upadhyay, A., 2021b. United States Shapefile download a free map – Boundary, County [WWW Document]. IGIS Map. URL https://www.igismap.com/united-states-shapefile-download-free-map-boundary-states-and-county/ (accessed 1.5.21).

Van Zyl, J., Kim, Y., 2011. Synthetic Aperture Radar Polarimetry, 1st ed. John Wiley and Sons Inc., New Jersey, https://doi.org/10.1002/9781118116104.

Vashishtha, A., Kumar, S., 2020. Characterization of geomorphological features of lunar surface using Chandrayaan-1 Mini-SAR and LRO Mini-RF data. Quat. Int. 1–20. https://doi.org/10.1016/j.quaint.2020.08.018.

Velotto, D., Bentes, C., Tings, B., Lehner, S., 2016. First Comparison of Sentinel-1 and TerraSAR-X Data in the Framework of Maritime Targets Detection: South Italy Case. IEEE J. Ocean. Eng. 41, 993–1006. https://doi.org/10.1109/JOE.2016.2520216.

Wang, F., Liu, A., Xu, H., Jiang, T., 2019. A Method for Estimating and Validating Polarimetric Distortion Parameters Using Corner Reflectors and Its Applicability Analysis. IEEE J. Sel. Top. Appl. Earth Obs. Remote Sens. 12, 5345–5359. https://doi.org/10.1109/JSTARS.2019.2959192.

Wang, S., Qi, H., Yu, W., 2009. Polarimetric SAR internal calibration scheme based on T/R module orthogonal phase coding. IEEE Trans. Geosci. Remote Sens. 47, 3969–3980. https://doi.org/10.1109/TGRS.2009.2018629.

Woodhouse, I.F., 2006. Introduction to Microwave Remote Sensing, first ed. TCRC, Press, Taylor & Francis, Boca Raton. https://doi.org/10.1201/9781315272573

Wright, P.A., Quegan, S., Wheadon, N.S., Hall, C.D., 2003. Faraday rotation effects on L-band spaceborne SAR data. IEEE Trans. Geosci. Remote Sens. 41, 2735–2744. https://doi.org/10.1109/TGRS.2003.815399.

Zhang, H., Li, Z., Fang, C., 2017. High-precision distortion parameters estimation for polarimetric SAR calibration. Electron. Lett. 53, 806–808. https://doi.org/10.1049/el.2017.1315.